Version R1

word count 9,021

Zn-clays in the Kihabe and Nxuu prospects (Aha Hills, Botswana): a XRD and TEM study

PUTZOLU FRANCESCO[1*], ABAD ISABEL[2], BALASSONE GIUSEPPINA[3], BONI MARIA[1,3], LUPO FRANCESCO[3], and MONDILLO NICOLA[1,3]

[1]Department of Earth Sciences, The Natural History Museum, Cromwell Road, London SW7 5BD, UK

[2]Departamento de Geología and CEACTEMA, Universidad de Jaén, Campus Las Lagunillas sn, 23071 Jaén, Spain

[3]Dipartimento di Scienze della Terra, dell'Ambiente e delle Risorse, Università degli Studi di Napoli Federico II, Complesso Universitario Monte S. Angelo, Via Cintia 26, 80126 Napoli, Italy

[4]Istituto Nazionale di Geofisica e Vulcanologia, Osservatorio Vesuviano - Sezione di Napoli, Via Diocleziano, 328, 80125 Napoli, Italy

* = francesco.putzolu1@nhm.ac.uk

ABSTRACT

Zinc clays are commonly found in oxidized Zn deposits and, even though they rarely represent the main target of the ore exploitation, they can be used as a proxy to restore the genetic conditions during ore-forming processes. This work sheds light on the micro- to nano-mineralogy and on the genesis of Zn-clays in the Kihabe and Nxuu prospects (located in the Aha Hills district, Northern Botswana), through an integrated XRD and TEM study of the mineralized facies occurring in the mineralized system. The Kihabe and Nxuu ores are hosted in a Neoproterozoic metamorphozed quartzwacke unconformably covered by the recent sedimentary rocks, also containing calcretes, of the Kalahari Group. In the analyzed samples, four distinct mineralogical facies have been recognized: *i.* vanadate-calcrete facies, poor of Zn-clays; *ii.* low Zn-clay facies, characterized mostly by clays showing low Zn concentrations; *iii.* Zn-clay facies, containing proper Zn clay minerals; *iv.* sulfide facies, devoid of Zn-clays. In all the facies detrital dioctahedral mica (muscovite and illite) is interstratified with smectite in the form of random (R0) to short-range ordered (R1) I/S, which locally shows significant Zn concentrations. In the sulfide facies kaolinite overgrowing onto mica packets has been detected. The low Zn-clay facies is dominated by Zn-bearing beidellite, with minor kaolinite and fraipontite. The Zn-clay facies consists mostly of a random (R0) interstratified clay between a 7-Å phase corresponding to fraipontite, and a 2:1 swelling clay component identifiable with the dioctahedral smectite, with minor sauconite.

The micro- to nanoscale paragenetic study performed by TEM indicates that the above-mentioned clays formed through a multistage process, eventually ending with the genesis of Zn-bearing phyllosilicates assemblages. The main steps were: *i.* alteration of detrital mica and dissolution of feldspar clasts, which led to the formation of epitaxial kaolinite and replacive beidellite; *ii*. fertilization of barren clays and formation of replacive to epitaxial fraipontite/smectite and of Zn-bearing mica, through input of Zn^{2+} deriving from sphalerite or willemite dissolution by mixed meteoric-hydrothermal fluids; *iii.* formation of low tetrahedral charge sauconite, either in pores or as replacement of K-feldspars under surficial hypersaline conditions, possibly also linked to the establishment of the arid climate in region. These processes provide insights into genesis of Zn-Pb-V ore deposits in northwest Botswana. Furthermore, the identification of a Zn-smectite species having a stevensite-like stoichiometry is valuable for future studies dealing with the systematics of clay minerals.

Keywords: Zn-clays; nonsulfide; XRD; TEM; fraipontite; Kihabe; Nxuu; Botswana.

INTRODUCTION

Nonsulfide ores are oxidized Zn>>Pb mineral systems that form through the supergene alteration of sulfide deposits (e.g., Mississippi Valley-type, Volcanic-hosted Massive Sulfides, Sedimentary Exhalative deposits etc.), or when oxidising hydrothermal to metamorphic fluids overprint pre-existing Zn ores (Large 2001; Boni and Mondillo 2015). Based on their main features, e.g., formation process, ore paragenesis etc., they are classified as: *i*. direct replacement type; *ii*. wall-rock replacement type; *iii.* karst-filling type (Hitzman et al. 2003). Supergene nonsulfides occur in siliciclastic to carbonate host-rocks. The main ore-carriers in supergene nonsulfides are carbonates (e.g., smithsonite, hydrozincite and cerussite), hydrosilicates (e.g., hemimorphite), and less sulfates, phosphates and vanadates (e.g., anglesite, tarbuttite and descloizite, respectively). Furthermore, the dissolution of aluminosilicates from siliciclastic rocks during the ore-formation process can result in the formation of various clay minerals, which may behave as effective sinks for valuable metals as Zn and Cu (Boni and Mondillo 2015 and references therein). Consequently, the occurrence of Zn-clays, either as subordinate phases (e.g., La Calamine, Belgium; Bou Arhous, Marocco; Bongarà, Perù; Coppola et al. 2008; Choulet et al. 2016; Balassone et al. 2020) or as prevailing ore minerals (e.g., Accha-Yanque, Peru; Skorpion, Namibia; Borg et al. 2003; Mondillo et al. 2015; Balassone et al. 2017), has been documented in several research

This is the peer-reviewed, final accepted version for American Mineralogist, published by the Mineralogical Society of America.
The published version is subject to change. Cite as Authors (Year) Title. American Mineralogist, in press.
DOI: https://doi.org/10.2138/am-2022-8439. http://www.minsocam.org/

papers over the last decades. Natural Zn-clays form in many environments under slightly acidic to neutral pH (Manceau et al. 2000; Juillot et al. 2003), although a wide range of experimental studies (e.g., Kloprogge et al., 1999, 2001; Higashi et al. 2002; Petit et al. 2008; Pascua et al. 2010) have shown that they can be synthetized under variable pH and temperature conditions (pH = 6 – 12 and T° = 20 – 200 °C). The proposed mechanisms of formation of Zn-clays are based on different paradigms, mostly deriving by their variable mode of occurrence within the textural ore components and by the different source of elements. Several authors (Boni et al. 2009; Choulet et al. 2016) proposed that both in siliciclastic and in carbonate systems, Zn-clays may have a supergene origin that results from the feldspar alteration in the siliciclastic lithologies or is originated through the alteration of the insoluble components (e.g., residual clays and/or illite) from the carbonate rocks. Other authors (e.g., Mondillo et al. 2015, 2020 Buatier et al. 2016) have suggested that Zn-clays may also form from metals-rich solutions under hydrothermal conditions, either during the emplacement of the sulfide bodies or in a distal alteration halo formed following the evolution of the chemico-physical features of the mineralizing fluids. Zinc-rich phyllosilicates (Table 1) can be classified in the following groups:

- Smectites, which are 15 Å-type 2:1 clay species, consisting of both tri- and dioctahedral phases. The trioctahedral end-member of the smectite group is represented by sauconite, a saponite-like phase bearing Zn as the main octahedral metal. Sauconite is the most common clay mineral in nonsulfide ores (Large 2001; Hitzman et al. 2003; Mondillo et al. 2015; Boni and Mondillo 2015), and is the major Zn-phase in the world-class Skorpion deposit in Namibia (Borg et al. 2003; Kärner 2006; Balassone et al. 2017; Schingaro et al. 2021). Sauconite commonly results from the hydrolysis of aluminosilicate minerals in supergene environment (Tiller and Pickering 1974; Harder 1977), although several studies on natural and synthetic Zn-smectites pointed out that it may also form under hydrothermal conditions (Mondillo et al. 2015). Dioctahedral smectites (e.g., beidellite and montmorillonite) may be also present in nonsulfides, although they typically have a significantly lower Zn grade compared to the trioctahedral end-member (e.g., Mondillo et al. 2015; Balassone et al. 2017);
- Fraipontite, a 7 Å-type 1:1 clay representing the Zn-rich trioctahedral counterpart of the kaolinite-serpentine group (serpentine subgroup), is one of the Zn-clays detected in the

This is the peer-reviewed, final accepted version for American Mineralogist, published by the Mineralogical Society of America.
The published version is subject to change. Cite as Authors (Year) Title. American Mineralogist, in press.
DOI: https://doi.org/10.2138/am-2022-8439. http://www.minsocam.org/

Moroccan High Atlas (Buatier et al. 2016; Choulet et al. 2016) and in the Bongarà (Perù) mining districts (Arfè et al. 2017; Balassone et al. 2021). In both cases its formation was explained by a direct precipitation process from hydrothermal to supergene metals-rich solutions;

- Baileychlore, a 14 Å-type 2:1:1 trioctahedral clay mineral, is the Zn-rich end-member of the chlorite group (Rule and Radkle, 1988; Lee and Xu, 2017). This rare Zn-clay species has been mostly observed so far in altered andesite (Smith 1985), in high-temperature systems as skarn deposit (i.e., Red Dome mine, Australia; Torrey et al. 1986) and in a few other localities (https://www.mindat.org/min-488.html). Furthermore, the occurrence of this Zn-rich chlorite, in association with smithsonite, has been reported by Mt Burgess Mining N.L. (2018) in the oxide zone of the Kihabe deposit in Botswana.
- Mica group clays, which are 10 Å-type phases, are ubiquitous in supergene nonsulfides. In these systems mica occurs mostly as detrital dioctahedral K-deficient muscovite (i.e., illite). Several authors (e.g., Balassone et al. 2017) have shown that mica, although containing minor Zn amounts, plays a pivotal role for the formation of later smectite and/or of illite – smectite mixed layers (I/S), as detrital mica packets may act as a structural template easing the nucleation of Zn-clays. Among the minerals of the mica group, hendricksite, a Zn-rich trioctahedral species, has been also observed in high-temperature magmatic to metamorphic environments, as well as in hypogene nonsulfides. In the former, trioctahedral Zn-micas has been observed in peralkaline volcanic rocks that experienced skarn conditions (Sharygin 2015). In nonsulfide ores, Zn-mica has been identified in the Franklin deposit (USA) and in the Bongarà district (Perù) (Hitzman et al. 2003; Balassone et al. 2020).

Mondillo et al. (2020) recently investigated the Kihabe and Nxuu nonsulfide prospects (Botswana) and described the emplacement mechanism of the hypogene and supergene Zn-Pb-V ores. In the Kihabe deposit (Botswana), Zn-clay minerals, preliminarily interpreted as baileychlore with subordinate sauconite and illite, have been recorded as distal alteration halo of base-metal sulfide ore (Mondillo et al. 2020). However, due to the size of the clay particles and intergrowths with other phases, a clear identification of Zn-bearing clay minerals of this deposit was complex and at times questionable. For

This is the peer-reviewed, final accepted version for American Mineralogist, published by the Mineralogical Society of America.
The published version is subject to change. Cite as Authors (Year) Title. American Mineralogist, in press.
DOI: https://doi.org/10.2138/am-2022-8439. http://www.minsocam.org/

instance, very low amounts of Fe in the supposed Zn-chlorite were detected by Mondillo et al. (2020) compared to the type locality occurrence (Rule and Radkle 1988). Therefore, in order to improve the definition of this clay minerals assemblage, we focused the present study on a chemical and microtextural characterization of the Zn clays minerals in the Kihabe and Nxuu areas using a combined XRD and TEM/HRTEM/STEM-HAADF analytical protocol, supplemented by SEM-EDS investigations. The final aim is to shed light on the nature of the Kihabe and Nxuu clays minerals, to discuss the genetic process responsible for their origin and to contribute to the knowledge of the clay minerals (which can trap economic metals) associated to ores. Indeed, a deep understanding of the mineralogical and chemical footprint of clays and their distribution plays a pivotal role in outlining the processing and metallurgical flowsheets and in identifying potential additional sources of valuable raw materials in the orebodies.

GEOLOGICAL SETTING

Regional geological framework

The Kihabe and Nxuu prospects are located in northwest Botswana, near the border between Botswana and Namibia, within the Ghanzi – Chobe zone (Fig. 1a,b), which is a NE-trending Meso- to Neoproterozoic belt. This geological domain, lying below the Kalahari sedimentary cover, was structured during the Damara Orogeny, after the inversion of the Northwest Botswana rift. The basement rocks mostly occur NW to the Ghanzi – Chobe zone and, according to Key and Ayers (2000) and Singletary (2003), can be classified in the following groups:

- the Kwando Complex, which are granitic gneisses of uncertain Precambrian age;
- a Neoproterozoic macro-domain, which is supposed to be the NW limb of the Damara belt. This domain consists of the following terranes: *i.* amphibolite and mafic schists of the Roibok Complex; *ii.* Neoproterozoic greenschist-facies metasediments and marbles of the Koanaka Group. Both these lithologies crop out in the Kihabe area, as well as in the Koanaka Hills; *iii.* igneous and meta-igneous rocks of the Chihabadum Complex, which have a supposed Neoproterozoic age; *iv.* the Neoproterozoic Aha Hills Formation, which comprehends chert-rich marble and dolostone with low metamorphic grade. This domain crops out in the study area (the Aha Hills), and it is correlated with the Namibian Otavi Group;

This is the peer-reviewed, final accepted version for American Mineralogist, published by the Mineralogical Society of America.
The published version is subject to change. Cite as Authors (Year) Title. American Mineralogist, in press.
DOI: https://doi.org/10.2138/am-2022-8439. http://www.minsocam.org/

- the basement units of the Paleoproterozoic Quangwadum Complex, which consists of granitic gneisses outcropping in the Northern sector of the Aha Hills;
- the meta-sedimentary rocks of the Xaudum and Tsodilo Hills groups, which are considered either Paleoproterozoic or Neoproterozoic in age (Key and Ayers 2000; Singletary et al. 2003). The Xaudum Group consists of low-metamorphic grade marbles, chert-rich carbonates, slates and quartzites, while in the Tsodilo Hills Group quartz–muscovite schists, meta-conglomerates, ferruginous quartzites and biotite-gneisses lithologies have been observed. Both groups can be correlated with the lithologies of the same age occurring in Namibia. Specifically, the Xaudum Group is correlated with the Nosib Group, while the Tsodilo Hills Group with the Chuos Formation of the Damara succession (Singletary et al. 2003).

The youngest rocks occurring in the Ghanzi – Chobe zone are still Neoproterozoic in age and consist of clastic to carbonate lithologies (Ghanzi Group), which are correlated with units cropping in SW Namibia (Tsumis and Nosib groups) (Killick 1983; Hoffman 1989; Schwartz et al. 1996; Wendorff, 2005).

Main features of the Kihabe and Nxuu ore bodies

The orebody at Kihabe has an elongated shape, with an average width of 27 m and a strike length of 2.4 km. The local sedimentary sequence from bottom to top consists of: *i.* barren dolostone, strongly deformed; *ii*. highly deformed quartzwacke belonging to the Aha Hills Formation, which is host for the mineralisation; *iii.* recent sedimentary rocks containing calcretes, which belong to the Kalahari Group and have a thickness ranging between 5 to 15 m (Key and Ayers 2000; Mondillo et al. 2020). Most of the Kihabe ore (ca. 75%) consists of primary sulfides, which according to Loxton (1981) and Mapeo (2007) may be genetically attributed either to the class of sedimentary-hosted massive sulfides (SHMS) or Mississippi Valley-type (MVT) deposits. The remaining part of the Kihabe ore has features in line with those of nonsulfide ores allegedly of supergene origin (Mapeo, 2007). According to a preliminary study by Mondillo et al. (2020), the Kihabe nonsulfides have been possibly classified in two main associations: *i.* willemite + Zn-bearing chlorite (baileychlore), of hydrothermal origin; *ii.* smithsonite + cerussite + Zn-Pb-phosphates and vanadates + sauconite + iodargyrite of supergene origin. The Nxuu prospect consists mainly of oxidized mineral phases, with only traces of remnant sulfides. In both

This is the peer-reviewed, final accepted version for American Mineralogist, published by the Mineralogical Society of America.
The published version is subject to change. Cite as Authors (Year) Title. American Mineralogist, in press.
DOI: https://doi.org/10.2138/am-2022-8439. http://www.minsocam.org/

prospects, variable amounts of V, as well as traces of Ag and Ge have been detected (Mt Burgess Mining N.L. 2020). As in Northern Namibia, the supergene alteration in this part of Botswana is genetically related to post-Gondwana erosional episodes and weathering (Late Cretaceous to Miocene) (Boni et al. 2007; Mondillo et al. 2020).

MATERIALS AND METHODS

For this study, a total of 17 clay-bearing samples were collected at different depths in the cores of nonsulfide ore at Kihabe and Nxuu (Table 2). The analyzed samples consisted of both mineralized quartzwacke of the Aha Hills Formation and sedimentary cover rocks with calcrete of the Kalahari Group.

The bulk-rock mineralogical composition was determined through X-ray diffraction analysis (XRD) with a Seifert GE ID3003 at the Dipartimento di Scienze della Terra, dell'Ambiente e delle Risorse (DiSTAR), Università degli studi di Napoli Federico II (Italy). The analyses were carried out with a CuKα radiation, Ni-filtered at 40 kV and 30 mA, 3–70° 2θ, step scan 0.02° and time 10 s/step. Prior to each analysis a silicon standard was used to refine the instrumental parameters.

The XRD study of the clay fraction was performed following the procedure described in Moore and Reynolds (1997). To obtain the fine-grained fraction ($\varphi < 2$ μm), each specimen was crushed and milled to obtain 30 g of powder with a grain size < 1 mm. Afterwards, about a quarter of the powdered sample was blended in deionized water to undergo disaggregation with an ultrasonic probe for 15 mins. Following the ultrasonic treatment, the clay fraction was obtained through four steps of progressive sedimentation (i.e., 1 min, 5 mins, 60 mins and 17 h). To avoid the potential flocculation of clays during the sedimentation steps, 3 g of sodium hexametaphosphate, $(NaPO_3)_6$, was added to the solution. Afterwards, two cycles of centrifugation (i.e., 5 min at 5000 rpm followed by 40 min at 8000 rpm) were carried out to further refine the separation of the fine fraction. After the last cycle of centrifugation, the precipitate was blended with 5 ml of deionized water and then smeared on glass slides and left drying at room T°. The latter step allowed the orientation of the clay packets along the (00l) crystallographic plane (air dried conditions). To test the occurrence of swelling clays and of mixed layers, the specimens were solvated with ethylene glycol, $C_2H_6O_2$, at 80 °C for 24 h. The identification of clays, through loss and/or modification of the crystal structure, was also carried out

This is the peer-reviewed, final accepted version for American Mineralogist, published by the Mineralogical Society of America.
The published version is subject to change. Cite as Authors (Year) Title. American Mineralogist, in press.
DOI: https://doi.org/10.2138/am-2022-8439. http://www.minsocam.org/

through heat treatments at 350 °C and 550 °C for 2 h and 1 h, respectively. Furthermore, to distinguish trioctahedral from dioctahedral clays and to classify the occurring polytypes, the precipitate from the first cycle of centrifugation was dried to prepare randomly oriented mounts using the side-loading procedure. This procedure was aimed to minimize the clay orientation along the (00l) plane, in order to detect the typical 06l and hkl bands (Moore and Reynolds 1997).

XRD analyses on clay aggregates and on randomly oriented clay mounts were performed at the Centro de Instrumentación Científico Técnica (CICT) of the Universidad de Jaén (Spain) using a PANalytical Empirean diffractometer equipped with an X'Celerator solid-state linear detector and θ/θ goniometer. The instrument operated with a CuKα radiation, 45 kV and 40 mA, step scan 0.01° and a total counting time of 10 s per step. The XRD pattern of clay aggregates were collected within the 3 – 35° 2θ range, while the randomly oriented mounts were analyzed in the range of 3 – 70° 2θ. A preliminary textural analysis was performed on standard thin sections (~30 μm) by transmitted light optical petrography and Scanning Electron Microscopy equipped with Energy Dispersive X-ray Spectroscopy (SEM-EDS). SEM analyses were carried out with a ZEISS Merlin VP instrument at the DiSTAR, and at the Centro de Instrumentación Científico-Técnica (CICT, Universidad de Jaén, Spain). TEM-HRTEM analysis was carried out on 6 specimens (i.e., K8, K21, K23, K25, K26 from Kihabe, and NX685 from Nxuu, Table 2). Samples K21, K23, K25, K26 and NX685 were selected as they best represent the nonsulfide ore types, while sample K8 was selected to check the clays characteristics in the sulfide ore as well. The micro- to nanofeatures of clays were assessed on ion-milled subsamples prepared at the Universidad de Jaén (Spain). To obtain the subsamples, Cu rings were attached to the areas of interest onto the thin sections prepared with Canada balsam. The detachment of the selected areas was conducted by heating and ion-thinning using a Fischione-1010 ion mill and further carbon coating. The ion milling involved a first treatment at 12°, 5 kV and 5 mA until the first hole opened, followed by two steps at 8°, 4 kV and 5 mA and at 5°, 3 kV and 5 mA. The TEM analyses were carried out at the Centro de Instrumentación Cientifica (CIC) of the Universidad de Granada (Spain), with the HAADF FEI TITAN G2 and the HAADF Thermo Fisher Scientific TALOS F200X microscopes. With both instruments the mineralogy, textures and paragenesis of clays were assessed by combining TEM with high-resolution TEM (HRTEM), scanning transmission electron microscopy (STEM), high-angle annular dark field (HAADF) and selected-area electron diffraction patterns (SAED). The nanoscale

This is the peer-reviewed, final accepted version for American Mineralogist, published by the Mineralogical Society of America.
The published version is subject to change. Cite as Authors (Year) Title. American Mineralogist, in press.
DOI: https://doi.org/10.2138/am-2022-8439. http://www.minsocam.org/

chemistry of clays was analyzed by energy dispersive X-ray microscopy (AEM-EDX) and compositional maps. The HAADF FEI TITAN G2 microscope operated at 300 kV and with a point-to point resolution of 0.08 nm in the TEM mode and 0.2 nm in the STEM mode. The HAADF Thermo Fisher Scientific TALOS F200X operated at 200 kV and with a point-to-point resolution of 0.12 nm in the TEM mode and 0.19 nm in the STEM mode. In both cases, the quantitative micro- to nano-chemical analyses were carried out in STEM mode through AEM-EDX (energy dispersive X-ray microscopy) by using the Super-X system. The quantitative AEM-EDX analyses were obtained using albite, biotite, muscovite, spessartine, olivine, titanite, and hemimorphite as standards, in compliance with the protocol proposed by Abad and Nieto (2003). This enabled obtaining the K-factors used for the intensity rations-to-concentration conversion (Cliff and Lorimer 1975). The chemical formulas of clay minerals were calculated following the stoichiometry by Newman and Brown (1987). Specifically, 22 negative charges [$O_{10}(OH)_2$] were used for 2:1 species (i.e., smectite and mica groups), while 14 negative charges [$O_5(OH)_4$] for 1:1 species (i.e., kaolinite-serpentine group). Iron was considered trivalent (Fe^{3+}) in dioctahedral clays and bivalent in trioctahedral clays (Fe^{2+}).

RESULTS

XRD analysis on bulk samples and clay separates, optical and scanning electron microscopy

For better understanding the mineralogical footprint of clays, XRD and petrographic analyses were conducted on both the host rocks (quartzwacke and calcrete) and the various ore types (Fig. 2, 3 and 4). Based on the mineralogical assemblages of the ore, four *facies* were recognized in the Kihabe and Nxuu prospects: *i.* vanadate-calcrete facies, *ii.* low-Zn-clays facies, *iii.* Zn-clays facies, and *iv.* sulfide facies. The latter was only considered in this study for TEM analyses on a single representative sample. In the following paragraphs we report the main results obtained through the XRD and petrographic analyses on the host rocks and the ore facies.

Host rocks

The clay-rich nonsulfide ore in the Kihabe and Nxuu prospects is hosted in quartzwacke and calcrete lithotypes. In the quartzwacke quartz is accompanied by subordinated calcite and K-feldspars. The phyllosilicates assemblage consists of smectite, mica and kaolinite-serpentine group clay minerals (Fig.

This is the peer-reviewed, final accepted version for American Mineralogist, published by the Mineralogical Society of America.
The published version is subject to change. Cite as Authors (Year) Title. American Mineralogist, in press.
DOI: https://doi.org/10.2138/am-2022-8439. http://www.minsocam.org/

256 2a). The quartzwacke has a blastopsammitic mylonitic texture consisting of medium-grained (up to 100
257 µm) quartz clasts, which are slightly deformed and surrounded by fine-grained (<10 µm) and
258 recrystallized quartz and mica (Fig. 4a,b). Scattered reddish clay minerals follow the tectonic foliation
259 (Fig. 4a), while Fe-oxy-hydroxides have a pseudomorphic texture likely inherited from the replacement
260 of former sulfides (Fig. 4b). Calcite, minor quartz, smectite and mica are the main phases occurring in
261 calcrete (Fig. 2a). In these rocks variable micro-fabrics have been observed, with calcite occurring in
262 two generations: late crystalline calcite filling voids and fractures (Fig. 4c,d) and micritic calcite
263 forming pseudo-ooidal aggregates (Fig. 4d). Quartz is present either as subangular clasts (100 µm to
264 >800 µm in size), or as fragments of recrystallized quartzite (Fig. 4c,d). Clay minerals occur as reddish
265 patches associated with late calcite (Fig. 4c).

266 *Vanadate-calcrete ore facies*

267 Descloizite, with subordinate vanadinite, is ubiquitous in the vanadate facies. Both minerals are either
268 present as late phases in the cement of the quartzwacke (Fig. 4e) or as prismatic to radial grains
269 associated with Pb-calcite and Zn-dolomite in the calcrete layers (Fig. 4f,g). Vanadates are also in close
270 association with Zn-bearing mica, which is the main clay species present in this ore type (Fig. 4h). The
271 occurrence of mica as dominant clay is confirmed by XRD analyses carried out on the fine-grained
272 fraction, where a 10 Å (00l of mica-group clays) non-swelling phase, which does not undergo any
273 structural modification after the heat-treatments, has been observed (Fig. 2b). According to XRD
274 analyses on randomly oriented mounts (Fig. 2c), it was determined that mica occurs as a dioctahedral
275 species (i.e., muscovite group) and is present in the form of the 1*M* e $2M_1$ polytypes. Furthermore, the
276 presence of a peak centred at 7 Å that disappears after treatment at 550°C, indicates the presence of a
277 phase belonging to the kaolinite-serpentine group (Fig. 2b).

278 *Low Zn-clays ore facies*

279 The low Zn-clay facies is dominated by quartz clasts showing an interlocking texture and partially
280 recrystallized rims, and by a relatively higher amount of feldspar. The phyllosilicates suite shows a ~14
281 Å phase, which shifts to ~17 Å after the ethylene glycol solvation, this pointing to the presence of clays
282 of the smectite group (Fig. 3a). Another major phase in the phyllosilicates suite is a 10 Å-spaced clay
283 (mica) that is refractory to any structural change both after solvation and heat treatments (Fig. 3a,b). In

This is the peer-reviewed, final accepted version for American Mineralogist, published by the Mineralogical Society of America.
The published version is subject to change. Cite as Authors (Year) Title. American Mineralogist, in press.
DOI: https://doi.org/10.2138/am-2022-8439. http://www.minsocam.org/

the ethylene glycol pattern (Fig. 3a), the position of the mica and smectite peaks in the 10 Å and 5 Å regions suggests that these phases occur in an interstratified clay mineral (illite/smectite, I/S), which has disordered structure (*Reichweite value* "R" = 0) and is dominated by the swelling component (% of illite in I/S<10%) (Moore and Reynolds 1997). Furthermore, minor reflections at ~7 Å and ~3.60 Å were also observed in air-dried mode (Fig. 3a). The disappearance of these peaks after heating at 550°C (Fig. 3b) confirms that kaolinite-serpentine group clays occur as a minor clay species. Important clues about the nature of smectite are given by the randomly oriented pattern (Fig. 3c), where peaks centred at 1.50 Å and 1.52 Å were observed. The former peak is typical of the 060 of a dioctahedral mica component (muscovite- to illite-like), while the latter falls in the typical range of the 060 of smectite clays.

In this facies, we observed that the K-feldspars are embedded as pre-tectonic porphyroblasts in a fine-grained matrix consisting of smectite>microcrystalline muscovite (Fig. 4i,j). Zinc-bearing smectites either replace K-feldspars (Fig. 4j,k) or incorporate the muscovite packets (Fig. 4l).

Zn-clays ore facies

In the Zn-clay facies the K-feldspars are relatively abundant and, alongside with quartz grains, are dispersed in a clayey matrix. The XRD traces show a clay minerals assemblage fairly similar to those observed in the low Zn-clay domain, with prevailing smectite, mica and clays of the kaolinite-serpentine group (Fig. 3d). However, in this facies the peaks occurring at 7.24 Å and 3.57 Å, characteristic of the 00l and 002 of 1:1 clays, after solvation with ethylene glycol underwent a shift toward 7.30 Å and 3.55 Å (Fig. 3e). This feature indicates the presence of an interstratified mineral between a swelling component (i.e., smectite) and a 7 Å mineral of the kaolinite-serpentine group (e.g., kaolinite, fraipontite or serpentine) (Moore and Reynolds 1997; Choulet et al. 2016). Based on the observed magnitude of the shift of the above peaks, this interstratified clay has a random structural packing (*Reichweite* value "R" = 0) and is dominated by the 7 Å non-swelling component (% of smectite <10%) (Moore and Reynolds 1997). Clues on the nature of the 7 Å clay are given by the spacings of the peaks in the 060 region of the randomly oriented pattern (Fig. 3f), where a peak at 1.54 Å points to a trioctahedral clay component. It is worth mentioning that the presence of residual quartz might theoretically contribute to this peak (211 of quartz centred at 1.54 Å). However, the 1.54 Å peak

This is the peer-reviewed, final accepted version for American Mineralogist, published by the Mineralogical Society of America.
The published version is subject to change. Cite as Authors (Year) Title. American Mineralogist, in press.
DOI: https://doi.org/10.2138/am-2022-8439. http://www.minsocam.org/

was not observed in other samples containing quartz and lacking trioctahedral clays (low Zn-clay facies, Fig. 3c), thus supporting the occurrence of trioctahedral 1:1 phyllosilicate. The high Zn-Al amounts detected through EDS analysis, suggest this clay is fraipontite. The absence of the diagnostic peak of kaolinite at 1.49 Å means that the latter phase may occur only in minor amounts compared to the trioctahedral Zn-rich counterpart. In this frame, the peak at about 1.50 Å is due to the 060 of dioctahedral phases as muscovite, with a possible minor contribution of the 061 of fraipontite (Fransolet and Bourguignon 1975, Choulet et al. 2016).

In the Zn-clay facies the clayey matrix displays darkish colours and fine-grained textures (Fig. 4m). Fraipontite occurs as a late phase in lath-shaped aggregates in voids between quartz grains (Fig. 4n), as replacement of K-feldspars (Fig. 4o) and as massive aggregates in association with Zn-bearing muscovite packets (Fig. 4p).

TEM-HRTEM and AEM – EDX study of clay minerals

The TEM study of the clay assemblage (Fig. 5 to 11) was carried out on selected samples, in order to adequately investigate nature and textures of the Zn-clay (i.e., sample K21, K23, K25 and K26) and low Zn clay (i.e., sample NX685) facies observed in the Kihabe and Nxuu prospects. The TEM observations were also performed on a specimen from the sulfide facies at Kihabe (i.e., sample K8).

Mineralogy and textures of clay minerals at the nanoscale

The application of the ion-milling preparation technique enabled the preservation of the mineral fabrics within the selected samples, which allowed determining the original textures of the Zn-clays and their paragenetic pathways.

In the Zn-clay facies, the phyllosilicates occur as stacked clay packages with a length between 10 nm to 500 nm and a width up to 1000 nm (Fig. 5a). In this facies, the dominant Zn-clay is a 1:1 phase with a 7 Å basal spacing (Fig. 5a-c), this confirming the fraipontite classification drawn by XRD on clay aggregates. Based on SAED pattern, HRTEM and EDX mapping, the fraipontite can be further classified in:

- *discrete* fraipontite: according to SAED and EDX mapping this Zn-clay species is associated with muscovite that has a 10 Å single layer periodicity (1*M* polytype) and kaolinite (Fig. 5a-c). This fraipontite type consists in mineralogically and chemically homogeneous domains

occurring as epitaxially nucleated packets onto pre-existing clays as kaolinite and muscovite (Fig. 5c,d). Furthermore, this kind of fraipontite is also locally associated with non-clay Zn-phases. Specifically, fraipontite was detected as a partial replacement of willemite grains (Fig. 5e,f).

- *interstratified* fraipontite: this Zn-clay species is either associated with muscovite (Fig. 6) or with K-feldspar (Fig. 7). In the former instance it occludes the cavities between detrital grains (Fig. 6a) and is locally in epitaxial relationship with muscovite packets (Fig. 6b). The EDX mapping shows that this fraipontite species bears significant amounts of Ca (Fig. 6c), which is the result of a fraipontite-based interstratified phase with a smectite clay component (F/S). Further clues about the F/S interstratified clay are given in Figure 7a-f, where fraipontite is present as a replacement product of K-feldspar grains. The HRTEM survey on a set of fraipontite packets shows the presence of the following crystallographic domains (Fig. 7c): *i.* a domain with 14 Å lattice fringes, which consist of a double layer stacking fraipontite; *ii.* a domain consisting of two stacking periodicities at 10 Å and 7 Å, which correspond to the 00l of collapsed smectite after interaction with the microscope vacuum and fraipontite, respectively. The detection of interlayered smectite- and fraipontite-type lattice fringes supports the XRD results on the clay fraction (Fig. 3d,e). Furthermore, F/S is not chemically homogenous, being characterized by an antagonism between Mg- and Zn-rich domains (Fig. 7d,e), and by minor Ca amounts (Fig. 7f).

TEM allowed detecting sauconite as a significant ore-carrier in the Zn-clay assemblage. Sauconite occurs as ca. 100 nm width compact clay packages (Fig. 8a-c) and is characterized by a 10 Å periodicity and an annular-shaped SAED pattern, indicating a high degree of turbostratic disorder (Fig. 8b). Unlike the Zn-smectites from Skorpion (Balassone et al. 2017) and from the Peruvian deposits (Mondillo et al. 2015), the sauconite of Kihabe and Nxuu rather than growing onto pre-existing muscovite, is found in cavities and as a replacement product of K-feldspar (Fig. 8d-f).

A low Zn dioctahedral smectite (beidellite) occurs as a minor species in the Zn-clay facies (Fig. 8c), while it is the dominant phase in the low Zn-clay facies (Fig. 9 and 10). Beidellite was formed through an epitaxial growth mechanism upon detrital muscovite and is often intimately associated with kaolinite

This is the peer-reviewed, final accepted version for American Mineralogist, published by the Mineralogical Society of America.
The published version is subject to change. Cite as Authors (Year) Title. American Mineralogist, in press.
DOI: https://doi.org/10.2138/am-2022-8439. http://www.minsocam.org/

(Fig. 9a-d). Based on chemical mapping (Fig. 9b), dioctahedral smectite appears to be the main Zn carrier in the assemblage of the low Zn clay facies. Furthermore, beidellite was locally found as replacement of detrital muscovite grains (Fig. 9e-h). A local beidellite-fraipontite paragenetic association was observed, with the Zn-rich clays being detected on the basis of their brighter contrast with the relatively Zn poorer beidellite (Fig. 10a). In the low Zn-clay facies, fraipontite occurs as a late thin layer superimposed on beidellite packets (Fig. 10a-c). On the other hand, in the Zn-clay facies, the fraipontite-beidellite assemblage was found in close association with detrital muscovite grains supporting the growth of the later clays (Fig. 10d,e). The chemical mapping and EDX spectra (Fig. 10f-i) on the newly formed clays-rich region shows that fraipontite and beidellite occur as intimately interlayered intergrowths, with fraipontite representing a later epitaxially nucleated species onto dioctahedral clay species.

In the sulfide facies of the deposit, Zn-phyllosilicates are absent and the clay assemblage is dominated by muscovite as compact clay packages (Fig. 11a,b). Muscovite is locally associated with kaolinite that occurs in epitactic contact with the edges of the muscovite layers (Fig. 11c-e), which is something that matches well with the kaolinite-muscovite textural relationship observed also in the Zn-clay facies (Fig. 5c,d).

Mineral chemistry through AEM

Representative structural formulae of the detected clay species are given in Tables 3 and 4, while Figure 12 shows their chemical variation based on the nanoscale AEM analysis. Fraipontite shows significant chemical variations, with the tetrahedral site dominated by Si (1.35 – 2.19 apfu, Fig. 12a), while Al^{IV} can be locally absent to values up to 0.65 apfu (Fig. 12b). Fraipontite from Nxuu forms a subset of data exceeding the 2 apfu cut-off value for the tetrahedral occupancy, which is a further indicator of the interstratification with a smectite clay component. Most of the octahedral site is occupied by Zn (1.21 – 2.69 apfu, Fig. 12c), followed by Al^{VI}, Mg and Fe (0.13 – 1.20 apfu Al, 0 – 0.61 apfu Mg, 0 – 0.18 apfu Fe, Fig. 12b-e). The Zn amount in fraipontite is anticorrelated with Al^{VI} and Mg (Fig. 12c,d). Trace amounts of interlayer cations, mostly Ca and K, were also detected with maximum values up to ca. 0.10 apfu (Fig. 12f).

This is the peer-reviewed, final accepted version for American Mineralogist, published by the Mineralogical Society of America.
The published version is subject to change. Cite as Authors (Year) Title. American Mineralogist, in press.
DOI: https://doi.org/10.2138/am-2022-8439. http://www.minsocam.org/

Sauconite has a Si content that locally fully occupies the tetrahedral site (4 apfu Si) and decreases progressively down to 3.01 apfu (Fig. 12a), with the remaining occupancy fulfilled by Al^{IV} (0 – 0.99 apfu, Fig. 12b). Zinc dominates the octahedral site, with values of 2.07 – 3.13 apfu. Octahedral Al is highly variable, being either absent or occurring as a major constituent (0 – 0.71 Al^{VI}, Fig. 12c), while Mg and Fe are generally low (0 – 0.16 apfu Fe and 0 – 0.24 apfu Mg, Fig. 12d,e). A major feature of the chemistry of sauconite is the dichotomy between the Zn and Al^{VI} concentrations (Fig. 12c). The interlayer site of sauconite is dominated by K, with minor amounts of Ca (up to 0.34 apfu K and 0.17 Ca, Fig. 12f). Most of the AEM data obtained on sauconite are characterized by a depletion of interlayer cation and of Al^{IV} if compared to the stoichiometric values.

Beidellite has a Si content between 2.89 and 3.98, while Al^{IV} amounts between 0.02 and 1.11 apfu (Fig. 12a,b). The main octahedral cation is Al^{VI} (0.69 – 2.02 apfu), followed by Zn, Fe and Mg (0.14 – 0.92 apfu Zn, 0.01 – 0.54 apfu Fe and 0.03 – 0.32 apfu Mg, Fig. 12b-e). The anticorrelation between Al^{VI} and Zn is the main chemical variation observed in beidellite (Fig. 12c). The main interlayer cation is K, followed by Ca (up to 0.23 apfu K and 0.18 Ca, Fig. 12f).

Mica-group clays (muscovite- and illite-like) have a variable composition, with Si and Al^{IV} ranging between 2.97 – 3.24 apfu and 0.76 – 1.03 apfu, respectively (Fig. 12a,b). In this frame, Al^{VI} is the main octahedral metal (1.51 – 1.94 apfu, Fig. 12b), although Zn locally shows high values (0 – 0.70 apfu, Fig. 12c) in Zn-bearing mica. Potassium is the dominant interlayer cation, with values up to 1.06 apfu, although in a large subset analyses it decreases down to 0.43 apfu indicating that most of muscovite is K-deficient and has then an illite-like composition (Fig. 12f).

Kaolinite from Kihabe – Nxuu has negligible Zn (0 – 0.07 apfu Zn, Fig. 12c) and shows a composition close to its nominal stoichiometry.

In the Zn/Al_{tot} vs. Si/Al_{tot} plot (Fig. 12g), positive correlations are observed for the major Zn-carriers (i.e., fraipontite and sauconite), indicating that although these phases are characterized by significant chemical variations, the Zn^{2+} enrichment is accompanied by a charge compensation aided by the varying amount of Al^{3+} in the tetrahedral and octahedral sites.

The $4Si\text{-}M^{+}\text{-}3R^{2+}$ diagram (Fig. 13) has been used as a tool to classify dioctahedral and trioctahedral clay species and to visualize chemical trends resulting from the presence of interstratifications between different phyllosilicate types (Meunier 2005). In this projection, the chemistry of fraipontite from

This is the peer-reviewed, final accepted version for American Mineralogist, published by the Mineralogical Society of America.
The published version is subject to change. Cite as Authors (Year) Title. American Mineralogist, in press.
DOI: https://doi.org/10.2138/am-2022-8439. http://www.minsocam.org/

Kihabe and Nxuu shows an off-set with its accepted stoichiometric composition and with fraipontite from Peruvian deposits (Balassone et al. 2020). This mismatch results from the displacement of our data toward higher values of the M^+ and 4Si indexes, leading to a slight overlap with the fraipontite data from Moroccan Zn ores (Choulet et al. 2016). A significant chemical drifting can be traced also for sauconite data, which form a trend from its typical stoichiometry (Balassone et al. 2017; Mondillo et al. 2015) toward very low values of the M^+ index. Our mica data do not match the field of Zn-bearing illite from the Skorpion and Peruvian deposits (Balassone et al. 2017; Mondillo et al. 2015). However, a chemical trend toward the 4Si axis might result from the minor presence of interstratifications with a dioctahedral 2:1 clay component (beidellite). This is something that is in good agreement with the detection of the I/S mixed layer through XRD on the clay fraction (Fig. 3a). Lastly, beidellite and kaolinite analyses from Kihabe and Nxuu fit well with data reported by previous authors, although for the former clay species a trend towards higher M^+ values, likely resulting from interstratification with mica, can be observed.

DISCUSSION

Zn-clays identification

The XRD and TEM data presented in this study provide new insights on the nature of the Zn-clay assemblage occurring in the nonsulfide ore of the Kihabe and Nxuu prospects, which differ from previous investigations carried out on the same deposits (Mondillo et al. 2020). Specifically, the reappraisal of the nature of clays performed by XRD on clay aggregates and TEM confirmed the presence of a Zn-rich trioctahedral 2:1 swelling clay (i.e., sauconite) and of a 2:1 non swelling clay species locally Zn-bearing (i.e., Zn-bearing muscovite to illite) and allowed the description of a Zn-rich dioctahedral 2:1 swelling clay (i.e., beidellite), which was not observed previously. The Zn-chlorite baileychlore, considered one of the most abundant minerals in the Kihabe ores, was not detected in the investigated samples. On the contrary, it was possible to identify fraipontite, a 7 Å trioctahedral clay with a berthierine-like structural configuration, representing the Zn-rich end-member of the kaolinite-serpentine group (Cesàro 1927; Brindley and Brown 1980). Considering that the compositions of baileychlore and fraipontite are characterized by the same sets of elements (i.e., Zn-Fe^{2+}-Al-Si-H_2O) and by the same stoichiometric ratio between the tetrahedral and octahedral sheets (i.e., $\sum_{oct} = 6$ and $\sum_{tet}$

This is the peer-reviewed, final accepted version for American Mineralogist, published by the Mineralogical Society of America.
The published version is subject to change. Cite as Authors (Year) Title. American Mineralogist, in press.
DOI: https://doi.org/10.2138/am-2022-8439. http://www.minsocam.org/

452 = 4 in baileychlore; $\sum_{oct}$ = 3 and $\sum_{tet}$ = 2 in fraipontite), it could be possible that the minerals were
453 misidentified in previous studies. In fact, by using the specific protocol for clay mineral identification
454 based on XRD on clay aggregates, it was possible to rule out the presence of chlorite species on the
455 basis of: *i.* the shifting of the 14 Å reflection towards higher *d*-spacings after the ethylene glycol
456 solvation, which is a feature of swelling clays of the smectite group; *ii.* the disappearance of the 7 Å
457 peak after heat treatment at 500 °C, that is a feature of kaolinite-serpentine group clays which under
458 this temperature conditions undergo endothermic dehydration ending with significant loss of structural
459 order (Insley and Ewell 1935; Bellotto et al. 1995). TEM analyses, that were then implemented to
460 associate the structural footprint of clays (by *in situ* SAED and HRTEM) with their chemical features
461 (by STEM – EDX), allowed to definitely determine that the 7 Å mineral belonging to the kaolinite-
462 serpentine group is the Zn-rich trioctahedral end-member (i.e., fraipontite). According to the
463 crystallographic and chemical features of fraipontite observed in this study, the 14 Å periodicity
464 detected with the HRTEM survey (Fig. 5f and 7c) has to be considered to be related to local double
465 layer stacking sequence of fraipontite, which is due to the intergrowth of different polytypes, as it was
466 already observed for the 2H1 polytype of cronstedtite case, a trioctahedral 1:1 clay belonging to the
467 kaolinite-serpentine group (Kogure et al. 2002), and for several fraipontite occurrences studied
468 elsewhere (Buatier et al. 2016).

469 **Nature of fraipontite**

470 Notable examples of fraipontite are the occurrences in Belgium (Coppola et al. 2008), in the Bongará
471 ore district, Peru (Arfè et al. 2017; Balassone et al. 2020) and in the Bou Arhous deposit, Morocco
472 (Buatier et al. 2016; Choulet et al. 2016). In the Bongará district, fraipontite is present as a chemically
473 and mineralogically homogenous phase in the form of late and well-crystallized pore-infills within
474 previously formed clays (Balassone et al. 2020). Conversely, the study on the Bou Arhous deposit
475 (Choulet et al. 2016) has shown that the fraipontite occurs as a replacement of barren clays with a
476 random interstratification (*Reichweite* value "R" = 0) and a 2:1 swelling component with a sauconite-
477 like chemistry. The above authors inferred that this interstratified mineral was dominated by the 7 Å
478 component, with a smectite amount of approximately 15 – 25%. Further HRTEM observations
479 conducted by Buatier et al. (2016) confirmed the stacking between 7 Å and 10 Å layers (i.e., fraipontite

This is the peer-reviewed, final accepted version for American Mineralogist, published by the Mineralogical Society of America.
The published version is subject to change. Cite as Authors (Year) Title. American Mineralogist, in press.
DOI: https://doi.org/10.2138/am-2022-8439. http://www.minsocam.org/

and collapsed smectite), although STEM – EDX analyses detected a composition close to that of discrete fraipontite. In our data, we observed several proxies supporting the occurrence of a fraipontite-smectite mixed layer, similar to the Moroccan case study. Specifically:

i. fraipontite-bearing samples are characterized by a slight shift of the 00l and 002 peaks of the 7 Å phases after the ethylene glycol saturation (Fig. 3e), which is a proxy of a random interstratification with a swelling phase;

ii. the HRTEM survey detected irregular stacking sequences between 7 Å and 10 Å lattice fringes (Fig. 7c);

iii. the STEM-EDX mapping of fraipontite-rich area recorded significant amounts of cations (i.e., Ca) that are typically hosted in the interlayer site of swelling clays (Fig. 6c and 7f);

iv. in the $4Si\text{-}M^{+}\text{-}3R^{2+}$ projection, the quantitative STEM – EDX data of fraipontite from Kihabe and Nxuu, due to relatively high values of the M^{+} index, are displaced from the nominal fraipontite chemistry that falls of the $4Si - 3R^{2+}$ axis (Fig. 13).

However, a notable difference in comparison with the Moroccan case study is represented by the features of the swelling component of the interstratified clay. In particular, according to our STEM – EDX data, the main chemical variation in fraipontite is the anticorrelation between the Zn amount and the $Mg - Al^{VI}$ pair (Fig. 7d,e and 12c,d). This indicates that in the Kihabe and Nxuu occurrences the smectite component of the interstratified clay has a low Zn montmorillonite-like chemical signature rather than a sauconite-like character.

Nature of sauconite

Sauconite, a Zn-rich saponite-like trioctahedral clay, was also observed in the analyzed set of samples. This phase is the most important Zn-ore mineral in the oxidized facies of several Zn deposits in Peru (Boni et al. 2009; Mondillo et al. 2015) and in Southern Africa (Borg et al. 2003; Balassone et al. 2017). However, some differences can be outlined between the sauconite from Kihabe and Nxuu and that from the above mining districts. According to XRD of sauconite-bearing samples, this clay species is present in Kihabe as a discrete phase, while in other districts it was observed also as interstratified phases either with mica or with 7 Å clays (e.g., Mondillo et al. 2015; Choulet et al. 2016). Furthermore, the STEM – EDX compositions of sauconite are characterized by variable values of the interlayer

This is the peer-reviewed, final accepted version for American Mineralogist, published by the Mineralogical Society of America.
The published version is subject to change. Cite as Authors (Year) Title. American Mineralogist, in press.
DOI: https://doi.org/10.2138/am-2022-8439. http://www.minsocam.org/

occupancy ($\sum_{int}$ = 0 – 0.41 apfu). On the stoichiometric standpoint, the local paucity of interlayer cations can be explained by the lack of Al^{IV} in some of the sauconite grains, which result in low levels of tetrahedral charge (i.e., low Si ⇌ Al^{IV} substitution) and in a negligible enrichment in monovalent cations (i.e., Na^{+} and K^{+}). Interestingly, this sauconite set of data shows a similar stoichiometry to stevensite, a trioctahedral phyllosilicate representing the low charge and R^{2+} cations-rich (i.e., Mg>>>Fe^{2+}) counterpart of saponite (Brindley and Brown 1980), which has the following ideal formula:

$$R_{2x}^{+}(Zn_{3-x}\square_{x})\ Si_4O_{10}(OH)_2$$

where □ represents site vacancies (Petit et al. 2008). Although this phase has never been detected in natural systems so far, several experimental studies managed to synthesize Zn-stevensite by simulating condition of low T (>80°C) hydrothermalism (Petit et al. 2008; Hildebrando et al. 2014) and to obtain Zn-stevensite by doping its naturally occurring Mg-rich counterpart under ambient temperature (Benhammou et al. 2005). Furthermore, as shown by the Zn vs. Al^{VI} and Zn/Al_{tot} vs. Si/Al_{tot} plots (Fig. 12c and g), a sauconite with low tetrahedral charge is the richest in Zn, with Zn values locally exceeding the stoichiometric values of the octahedral occupancy of trioctahedral smectites (i.e., Zn up to 3.31 apfu). Although the above observations might be a potential proxy of a possible Zn speciation in the interlayer site, several recent studies carried out through cation-exchange capacity (CEC) experiments, showed that Zn^{2+} is hosted in the octahedral sheet rather than in the interlayer site (Choulet et al. 2016; Schingaro et al. 2021).

Genesis of clay minerals in the Kihabe and Nxuu prospects

Preliminary genetic clues concerning the Zn-clay assemblage in the Kihabe deposit were provided by Mondillo et al. (2020), who attributed the formation of the non-swelling Zn-clay species, and their association with a kaolinite>galena assemblage, to the migration of the hydrothermal fluids from the Zn sulfide-bearing feeder zone and to their evolution towards high Eh conditions. Conversely, sauconite was considered to be the product of a later mineralizing stage of a possible supergene nature. The micro- to nanoscale TEM data presented in this study provided additional insights that enabled to unravel the paragenetic pathways (Fig. 14) ending with the formation of the Zn-clay assemblage. The earliest clay formation stage is represented by the alteration processes affecting K-feldspars and mica,

This is the peer-reviewed, final accepted version for American Mineralogist, published by the Mineralogical Society of America.
The published version is subject to change. Cite as Authors (Year) Title. American Mineralogist, in press.
DOI: https://doi.org/10.2138/am-2022-8439. http://www.minsocam.org/

which resulted in the formation of kaolinite and beidellite. These clay species were detected also in the sulfides and low Zn clays facies, which are in turn characterized by the paucity of Zn-clays and thus mostly likely record the minerogenetic processes occurred prior to the Zn fertilization of phyllosilicates. The TEM imaging evidenced that early kaolinite fills the porosity and lacks deformation features, meaning that the clay-formation process started after the most recent orogenic event recorded in the region (i.e., the Damara Orogeny; Schneider et al. 2008). The beidellite formation occurred both through epitaxial growth (Fig. 9b) and replacement of mica (Fig. 9g). Kaolinite was found to epitaxially grow upon the {001} cleavage planes of mica packets (Fig. 11c), meaning that the latter phase solely acted as a structural template allowing the nucleation of the newly formed clay, and as a replacement of beidellite (Fig. 9e-h). The observed difference in the minerogenetic process can be explained by considering that the kaolinitization of smectite is more feasible than that of mica, due to the layer charge and higher swelling properties of smectites, which favour the stripping of the tetrahedral sheet and render both the internal and external surfaces of the clay precursor potential alteration sites (Li et al. 2020 and references therein). The occurrence of authigenic kaolinite onto mica packets and the partial dissolution of mica when altered to beidellite are also a good proxy for the environmental conditions occurring in the preliminary stages of the clay formation. Specifically, the formation of authigenic kaolinite onto pristine mica requires acidic solutions plus Si^{4+} and Al^{3+}. These elements can be supplied to the system by the dissolution of K-feldspars (that are clearly altered in our samples, see Fig. 7), aided by the interaction with solutions rich in H^+ and/or H_3O^+. Considering that in meteoric waters Al^{3+} is among the most stable (immobile) species, a mixing with a hydrothermal fluid component is commonly required to transport this metal and to develop these processes. Experimental studies demonstrated that under hydrothermal and acidic conditions (T = 250 °C and pH = 3) the kaolinite formation using mica and smectite as a template is closely related to the presence of Al^{3+} in solution (Li et al. 2020). Other clues indicating the possible mixing of meteoric waters with high T fluids are given by the occurrence of partially altered mica grains. This is a common alteration feature resulting from the interaction with low pH (4 – 5.8) and relatively high T° (>90°C) fluids that favour the mica dissolution via exchange between interlayer cations and hydronium ($K^+ \rightleftharpoons H_3O^+$) (Lamarca-Irisarri et al. 2019).

This is the peer-reviewed, final accepted version for American Mineralogist, published by the Mineralogical Society of America.
The published version is subject to change. Cite as Authors (Year) Title. American Mineralogist, in press.
DOI: https://doi.org/10.2138/am-2022-8439. http://www.minsocam.org/

In this frame, Zn was supplied to the system either through dissolution of Zn sulfides and/or willemite. The timing of Zn-enrichment in the clay species can be subdivided in an early and a later stage. During the early stage, fraipontite formed after K-feldspar alteration and mineral nucleation onto pre-existing phases like mica, kaolinite and beidellite (Fig. 14). The K-feldspar-to-fraipontite transformation likely occurred via a dissolution–crystallization process under long-lasting acidic conditions (pH ~ 5), promoted by the paucity of carbonates in the host-rock and thus by low degree of pH buffering. The acidic conditions occurring at this stage, alongside with low $pCO_{2(g)}$ and high Si and Al activity, can explain both the congruent dissolution of the feldspar precursor and the Zn^{2+} fixation in fraipontite, rather than in hemimorphite and sauconite (Choulet al. 2014). The fraipontite overgrowing onto pre-existing dioctahedral species is similar to the Zn-clay formation reported by Choulet et al. (2016) for the nonsulfide ores from Morocco. The latter authors described this process as a fertilization of barren residual clays through an addition of Al^{3+} and Zn^{2+} to the system, involving both meteoric and low T hydrothermal fluids. This process was also confirmed by the isotopic study of Buatier et al. (2016). Our data suggest that Zn clays at Kihabe and Nxuu could have formed through a similar genetic process. However, the big difference with the Moroccan ores seems to be represented by the precursor clay for fraipontite. Choulet et al. (2016) inferred that Al^{3+} was mainly sourced by kaolinite dissolution in the Bou Arhous occurrence. In the Kihabe and Nxuu samples, instead, kaolinite appears unaltered contrarily to beidellite, which is commonly replaced by fraipontite: this suggests that beidellite would be the parent material for the replacive fraipontite, formed after the metal input process. In particular the fraipontite/smectite mixed layer might be the intermediate stage in the Zn-fertilization of beidellite (Fig. 10c, f and g). Evidence of this process is the dioctahedral and low Zn nature of the 2:1 swelling component of the interstratified clay, which may represent a relic of the beidellite precursor (Fig. 7d,e). The occurrence of Zn-bearing dioctahedral mica (muscovite- to illite-like), although as a minor layered silicate component, provides additional insights into the formation pathways of the clay assemblage in the Kihabe and Nxuu prospects. Specifically, the Zn enrichment of mica is commonly referred as being a proxy to the contribution of relatively high T fluids during the mineralizing process (Paradis et al. 2007; Sharygin, 2015; Balassone et al. 2020). Another proxy of possible thermal conditions governing the mica formation, is given by the detection of both random and short-range ordered I/S mixed layers (R0 and R1, respectively), which evidences that mica experienced environmental conditions increasing

This is the peer-reviewed, final accepted version for American Mineralogist, published by the Mineralogical Society of America.
The published version is subject to change. Cite as Authors (Year) Title. American Mineralogist, in press.
DOI: https://doi.org/10.2138/am-2022-8439. http://www.minsocam.org/

its structural order. According to previous studies (e.g., Nieto et al. 1996; Meunier 2005; Vázquez et al. 2014; Balassone et al. 2020), the R0 I/S-to-R1 I/S transition can be achieved under hydrothermal to diagenetic conditions in a thermal range between 75 and 120 °C. Concerning the origin of Zn-bearing mica, no particular relationship has been observed with any precursor phase, thus indicating that the most likely mechanism for metals enrichment is the mica to Zn-bearing mica solid state transformation process.

Sauconite was observed as the last phase in the Zn-clay assemblage, either as interstices filling within detrital grains or as a replacement of feldspars (Fig. 8c and f). These features are in good agreement with previous observations, that ascribed the formation of Zn-smectite to a late mineralizing stage in a surficial setting (Mondillo et al. 2020). Our new data, and in particular the chemical analogies of sauconite with stevensite, provide additional clues about the timing and conditions of formation for the Zn-smectite in the Kihabe and Nxuu prospects. Specifically, it is well-known that stevensite is one of the major authigenic phases in hypersaline and arid settings (Brindley and Brown 1980 and references therein; Chagas et al. 2016). As a consequence, the environment of formation of sauconite at Kihabe and Nxuu could have been significantly different from that of fraipontite and likely characterized by neutral to slightly basic pH and possibly higher $pCO_{2(g)}$. These conditions would fit with the presence of iodine-rich phases (e.g., Ag-iodide) in the Kihabe deposit (Mondillo et al. 2020) and with the occurrence of vanadate mineralisation in the Kalahari sedimentary cover (Fig. 4e-h). These mineral assemblages are typically formed in hypersaline environments and when the meteoric waters become enriched in dissolved carbonates species (Boni et al. 2007; Sillitoe 2009). Accordingly, these late stages of Zn-clay formations could be related with the humid-to-arid climatic shift that occurred in southern Africa during mid-Miocene (Partridge and Maud 1987; Van der Wateren and Dunai, 2001).

IMPLICATIONS

This study has relevant implications because it shed new light on genetic processes allowing the formation of Zn-bearing clays in Zn ore deposits. The main Zn-bearing phyllosilicate detected in the studied samples is fraipontite, together with minor amount of sauconite. With this study, it was determined that fraipontite clearly formed at the expenses of early precipitated barren phyllosilicates of hydrothermal origin, i.e., beidellite, that were fertilized by Zn^{2+} and Al^{3+}-rich fluids of mixed meteoric

This is the peer-reviewed, final accepted version for American Mineralogist, published by the Mineralogical Society of America.
The published version is subject to change. Cite as Authors (Year) Title. American Mineralogist, in press.
DOI: https://doi.org/10.2138/am-2022-8439. http://www.minsocam.org/

and low-T hydrothermal origin. Zn^{2+} was sourced by the dissolution of pre-existing Zn-species, i.e., sphalerite and/or willemite. Fraipontite formation can be explained either through the replacement of previously formed phases (e.g., beidellite) or by its nucleation from solutions following an epitaxial growth mechanism. The environmental conditions allowing the formation and stability of this Zn-clay require low pH (ca. 5), high Si and Al activity and low amounts of dissolved carbonate species in solution. At the same time, sauconite mostly derived from the alteration of K-feldspars and shows microtextural paragenetic and chemical features pointing to a later formation stage. The detection of a low tetrahedral charge and R^{3+}-depleted stevensite-like sauconite could be a proxy for the formation of this clay species under supergene arid conditions.

The above information sheds new light on the genesis of the Zn-Pb-V deposits of northwest Botswana that, occurring in the eastern extension of the Namibian Damara orogen, can be compared with similar deposits of the Namibian Otavi Mountainland. Considering that previous studies (Mondillo et al., 2020) proposed that sulfides formed before the Damara orogeny in the region (540-520 Ma), whereas willemite formed during the waning stages of the Damara Orogeny (490 Ma), fraipontite must have formed later than previous two phases. Because clay textures are compatible with mixed hydrothermal-supergene settings, fraipontite could have formed since Late Cretaceous, when the region was largely exhumed and dissected by normal faults possibly allowing the circulation of surficially-sourced hydrothermal fluids (Partridge and Maud, 1987). Sauconite instead should be genetically related to the humid-to-arid climatic transition, which occurred in the area since the Late Miocene (Partridge and Maud, 1987). The nature and the paragenesis of the Zn-bearing clays have an impact on the mineral exploration strategies because they control, for example, the distribution of the minerals in the orebodies. In this case, supergene Zn-clays should be located only in the more surficial zones of the mineralized sections.

Regarding the mineralogy of clays, the stoichiometric analogies between the stevensite-like sauconite occurring in the Kihabe and Nxuu prospects and the synthetic Zn-stevensite obtained in laboratory conditions (Benhammou et al. 2005; Petit et al. 2008; Hildebrando et al. 2014) add valuable hints to future studies dealing with the Zn enrichment in smectites, and can open new paths in the systematics of clay minerals.

ACKNOWLEDGMENTS

The authors are indebted to Mt. Burgess Mining N.L., and to N. Forrester, who provided the samples for this study. They are also grateful to C. de la Prada Sánchez and M.M. Abad-Ortega (CIC, Granada) for the support during TEM analyses, to R. de Gennaro (DiSTAR, Napoli) for his assistance during SEM analyses and to the technical and human support provided by CICT of Universidad de Jaén (UJA, MINECO, Junta de Andalucía, FEDER) during the XRD and SEM work and ion milling preparation for the TEM study. The authors wish to thank Fernando Nieto (CIC, Granada) for useful discussions and for inspiring us in the pursuit of clay mineral studies. We also thank Warren Huff for the editorial handling of the manuscript and two anonymous reviewers for providing useful insights that greatly enhanced the quality of the paper.

FUNDING

This research was supported by PhD student travel and research programme granted by the University of Napoli Federico II (Italy) to F. Putzolu, by the research project PGC2018-094573-B-I00 from the MCIN/AEI/10.13039/501100011033/-FEDER and the Research Group RNM-325 of the Junta de Andalucía, and by University of Napoli Federico II departmental research funds granted to N. Mondillo. Some partial support was also given by Mt. Burgess M.L. funds.

REFERENCES CITED

Abad, M.M., and Nieto, F. (2003). Quantitative EDX analysis in TEM. Practical development, limitations and standards. In: A. Mendez-Vilas, Ed., Science, Technology and Education of Microscopy: An Overview, 687–694. Badajoz, Spain, Formatex.

Arfè, G., Mondillo, N., Balassone, G., Boni, M., Cappelletti, P., and Di Palma, T. (2017). Identification of Zn-bearing micas and clays from the cristal and Mina Grande zinc deposits (Bongará Province, Amazonas Region, Northern Peru). Minerals, 7(11), 214. https://doi.org/10.3390/min7110214

Arostegui, J., Irabien, M.J., Nieto, F., Sangüesa, J., and Zuluaga, M.C. (2001). Microtextures and the origin of muscovite-kaolinite intergrowths in sandstones of the Utrillas Formation, Basque Cantabrian Basin, Spain. Clays and Clay Minerals, 49(6), 529-539.

Balassone, G., Nieto, F., Arfè, G., Boni, M., and Mondillo, N. (2017). Zn-clay minerals in the Skorpion Zn nonsulfide deposit (Namibia): Identification and genetic clues revealed by HRTEM and AEM study. Applied Clay Science, 150, 309-322. https://doi.org/10.1016/j.clay.2017.09.034

Balassone, G., Scognamiglio, V., Nieto, F., Mondillo, N., Boni, M., Cappelletti, P., and Arfè, G. (2020). The nature of Zn-phyllosilicates in the nonsulfide Mina Grande and Cristal zinc deposits (Bongará District, Northern Peru): The TEM-HRTEM and AEM perspective, American Mineralogist, 105(8), 1223-1241. https://doi.org/10.2138/am-2020-7140

Bellotto, M., Gualtieri, A., Artioli, G., and Clark, S.M. (1995). Kinetic study of the kaolinite-mullite reaction sequence. Part I: kaolinite dehydroxylation. Physics and Chemistry of Minerals, 22(4), 207-217.

Benhammou, A., Yaacoubi, A., Nibou, L., and Tanouti, B. (2005). Study of the removal of mercury (II) and chromium (VI) from aqueous solutions by Moroccan stevensite. Journal of Hazardous Materials, 117(2-3), 243-249. https://doi.org/10.1016/j.jhazmat.2004.09.023

Boni, M., Balassone, G., Arseneau, V., and Schmidt, P. (2009). The nonsulfide zinc deposit at Accha (Southern Peru): geological and mineralogical characterization. Economic Geology, 104(2), 267-289. https://doi.org/10.2113/gsecongeo.104.2.267

Boni, M., and Mondillo, N. (2015). The “Calamines” and the “Others”: The great family of supergene nonsulfide zinc ores. Ore Geology Reviews, 67, 208-233. https://doi.org/10.1016/j.oregeorev.2014.10.025

Borg, G., Kärne , K., Buxton, M., Armstrong, R., and Merwe, S.W.V.D. (2003). Geology of the Skorpion supergene zinc deposit, southern Namibia. Economic Geology, 98(4), 749-771. https://doi.org/10.2113/gsecongeo.98.4.749

Brindley, G.W., and Brown, G. (1980). Quantitative X-ray mineral analysis of clays. Crystal structures of clay minerals and their X-ray identification, 5th ed., 495 p. Mineralogical Society of Great Britain and Ireland, Great Britain.

Brugger, J., McPhail, D. C., Wallace, M., and Waters, J. (2003). Formation of willemite in hydrothermal environments. Economic Geology, 98(4), 819-835. https://doi.org/10.2113/gsecongeo.98.4.819

Buatier, M., Choulet, F., Petit, S., Chassagnon, R., and Vennemann, T. (2016). Nature and origin of natural Zn clay minerals from the Bou Arhous Zn ore deposit: Evidence from electron microscopy (SEM-TEM) and stable isotope compositions (H and O). Applied Clay Science, 132, 377-390. https://doi.org/10.1016/j.clay.2016.07.004

Cesàro, G. (1927). Sur la fraipontite, silicate basique hydraté de zinc et d'aluminum. Annales Societe Geologique Belgique, 50, 106–110 (in French).

Chagas, A.A., Webb, G.E., Burne, R.V., and Southam, G. (2016). Modern lacustrine microbialites: towards a synthesis of aqueous and carbonate geochemistry and mineralogy. Earth-Science Reviews, 162, 338-363. https://doi.org/10.1016/j.earscirev.2016.09.012

Choulet, F., Charles, N., Barbanson, L., Branquet, Y., Sizaret, S., Ennaciri, A., Brada, L., and Chen, Y. (2014). Non-sulfide zinc deposits of the Moroccan High Atlas: multi-scale characterization and origin. Ore Geology Reviews, 56, 115-140. https://doi.org/10.1016/j.oregeorev.2013.08.015

Choulet, F., Buatier, M., Barbanson, L., Guégan, R., and Ennaciri, A. (2016). Zinc-rich clays in supergene non-sulfide zinc deposits. Mineralium Deposita, 51(4), 467-490. https://doi.org/10.1007/s00126-015-0618-8

Cliff, G., and Lorimer, G.W. (1975). The quantitative analysis of thin specimens. Journal of Microscopy, 103, 203–207.

Coppola, V., Boni, M., Gilg, H.A., Balassone, G., and Dejonghe, L. (2008). The "calamine" nonsulfide Zn–Pb deposits of Belgium: petrographical, mineralogical and geochemical characterization. Ore Geology Reviews, 33, 187–210. https://doi.org/10.1016/j.oregeorev.2006.03.005

Ewell, R.H., and Insley, H. (1935). Hydrothermal synthesis of kaolinite, dickite, beidellite and nontronite. Journal of Research of the National Institute of Standards and Technology, 15, 173-186.

Fransolet, A.M., and Bourguignon, P. (1975). Données nouvelles sur la fraipontite de Moresnet (Belgique). Bulletin de la Société française de Minéralogie et de Cristallographie, 98(4), 235-244 (in French).

Hanson, R.E. (2003). Proterozoic geochronology and tectonic evolution of southern Africa. Geological Society, London, Special Publications, 206, 427–463. https://doi.org/10.1144/GSL.SP.2003.206.01.20

Harder, H. (1977). Clay mineral formation under lateritic weathering conditions. Clay Minerals, 12(4), 281-288.

Higashi, S., Miki, K., and Komarneni, S. (2002). Hydrothermal synthesis of Zn-smectites. Clays and Clay Minerals, 50(3), 299-305. https://doi.org/10.1346/00098600260358058

Hildebrando, E.A., Silva-Valenzuela, M.G., Neves, R.F., and Valenzuela-Diaz, F.R. (2014. Synthesis and characterization of smectite clay Zn-stevensite. Cerâmica, 60, 273-278. https://doi.org/10.1590/S0366-69132014000200017

Hitzman, M.W., Reynolds, N.A., Sangster, D.F., Allen, C.R., and Carman, C.E. (2003). Classification, genesis, and exploration guides for nonsulfide zinc deposits. Economic Geology, 98(4), 685-714. https://doi.org/10.2113/gsecongeo.98.4.685

Hoffman, K.H. (1989). New aspects of lithostratigraphic subdivision and correlation of Late Proterozoic to Early Cambrian rocks of the southern Damara Belt and their correlation with the central and northern Damara Belt and the Gariep belt. Communications of the Geological Survey of Namibia, 5, 59–67.

Jacquat, O., Voegelin, A., Juillot, F., and Kretzschmar, R. (2009). Changes in Zn speciation during soil formation from Zn-rich limestones. Geochimica et Cosmochimica Acta, 73, 5554–5571. https://doi.org/10.1016/j.gca.2009.05.069

Jerzykowska, I., Majzlan, J., Michalik, M., Göttlicher, J., Steininger, R., Clachowski, A., and Ruebenbauer, K. (2014). Mineralogy and speciation of Zn and As in Fe-oxide-clay aggregates in the mining waste at the MVT Zn-Pb deposits near Olkusz, Poland. Geochemistry, 74, 393–406. https://doi.org/10.1016/j.chemer.2014.03.003

752 Juillot, F., Morin, G., Ildefonse, P., Trainor, T.P., Benedetti, M., Galoisy, L., Calas, G., and Brown Jr,
753 G.E. (2003). Occurrence of Zn/Al hydrotalcite in smelter-impacted soils from northern France:
754 Evidence from EXAFS spectroscopy and chemical extractions. American Mineralogist, 88(4), 509-526.
755 https://doi.org/10.2138/am-2003-0405

756 Kärner, K. (2006). The metallogenesis of the Skorpion non-sulfide zinc deposit, Namibia. 252 p. Ph.D.
757 Thesis, Martin Luther University Halle-Wittenberg.

758 Key, R., and Ayers, N. (2000). The 1998 Edition of the Geological Map of Botswana. Journal of
759 African Earth Sciences, 30, 427–451. https://doi.org/10.1016/S0899-5362(00)00030-0

760 Killick, A.M. (1983). A preliminary account of the geology of the Kamtsas Formation of the Damara
761 Sequence, eastern Gobabis District, South West Africa/Namibia. South African Journal of Geology, 86,
762 11–18.

763 Kloprogge, J.T., and Frost, R.L. (1999). Infrared emission spectroscopic study of the dehydroxylation
764 of synthetic Mg/Al and Mg/Zn/Al-hydrotalcites. Physical Chemistry Chemical Physics, 1(7), 1641-
765 1647. https://doi.org/10.1039/A808496C

766 Kloprogge, J.T., Hickey, L., and Frost, R.L. (2001). Heating stage Raman and infrared emission
767 spectroscopic study of the dehydroxylation of synthetic Mg-hydrotalcite. Applied Clay Science, 18(1-
768 2), 37-49. https://doi.org/10.1016/S0169-1317(00)00028-4

769 Kogure, T., Hybler, J., and Yoshida, H. (2002). Coexistence of two polytypic groups in cronstedtite
770 from Lostwithiel, England. Clays and Clay Minerals, 50, 504–513.
771 https://doi.org/10.1346/000986002320514226

772 Lamarca-Irisarri, D., Van Driessche, A.E., Jordan, G., Cappelli, C., and Huertas, F.J. (2019). The Role
773 of pH, Temperature, and NH4+ during Mica Weathering. ACS Earth and Space Chemistry, 3(11),
774 2613-2622. https://doi.org/10.1021/acsearthspacechem.9b00219

775 Large, D. (2001). The geology of non-sulfide zinc deposits: An overview. Erzmetall, 54, 264-276.

776 Li, S., He, H., Tao, Q., Zhu, J., Tan, W., Ji, S., Yang, Y., and Zhang, C. (2020). Kaolinization of 2: 1
777 type clay minerals with different swelling properties. American Mineralogist, 105(5), 687-696.
778 https://doi.org/10.2138/am-2020-7339

779 Lee S., and Xu H. (2017). Powder XRD and TEM study on crystal structure and interstratification of
780 Zn-chlorite (baileychlore). Powder Diffraction, 32 (2), 118-123.
781 https://doi.org/10.1017/S088571561700041

782 Loxton, R.F. (1981). A Photogeological Study of the Aha Hills, Northwest Botswana; Loxton, Hunting
783 and Associates, Report for Billiton Botswana (Pty) Ltd: Gaborone, Botswana, 1981; p. 27.

784 Manceau, A., Lanson, B., Schlegel, M.L., Harge, J.C., Musso, M., Eybert-Berard, L., Hazemann, J.L.,
785 and Lamble, G.M. (2000). Quantitative Zn speciation in smelter-contaminated soils by EXAFS
786 spectroscopy. American Journal of Science, 300(4), 289-343. https://doi.org/10.2475/ajs.300.4.289

787 Mapeo, R.B. (2007). Geological and Structural Analysis of the Kihabe Base Metal Prospect in NW
788 Botswana. Internal Report for Mount Burgess (Botswana) (Pty) Ltd: Gaborone, 41 p. Botswana.

789 Meunier, A. 2005 Clays, Springer-Verlag, 472 p.

790 Mindat.org. www https://www.mindat.org/min-488.htm (accessed on November 2021).

791 Mondillo, N., Nieto, F., and Balassone, G. (2015). Micro-and nano-characterization of Zn-clays in
792 nonsulfide supergene ores of southern Peru. American Mineralogist, 100(11-12), 2484-2496.
793 https://doi.org/10.2138/am-2015-5273

794 Mondillo, N., Boni, M., Balassone, G., Forrester, N., Putzolu, F., and Santoro, L. (2020). Mineralogy
795 and Genesis of the Kihabe Zn-Pb-V Prospect, Aha Hills, Northwest Botswana. Minerals, 10(8), 685.
796 https://doi.org/10.3390/min10080685

797 Moore, D.M., and Reynolds, R.C. (1997). X-ray Diffraction and the Identification and Analysis of Clay
798 Minerals. Oxford University Press, 400 p. New York, NY, USA.

799 Mount Burgess Mining N.L. http://www.mountburgess.com (accessed on 1 July 2020).

800 Mount Burgess Mining N.L., 2018. Annual Report for the Year ended 30 June 2018. 51.

Newman, A.C.D., and Brown, G. (1987). Chemistry of Clays and Clay Minerals. Mineralogical Society, Monograph 6, 480 p. London.

Nieto, F., Ortega-Huertas, M., Peacor, D.R., and Aróstegui, J. (1996). Evolution of illite/smectite from early diagenesis through incipient metamorphism in sediments of the Basque-Cantabrian basin. Clays and Clay Minerals, 44, 304–323.

Paquet H., Colin F., Duplay J., Nahon D., and Millot G. (1986). Ni, Mn, Zn, Cr - smectites, early and effective traps for transition elements in supergene ore deposits. In: Rodriguez-Clemente R, Tardy Y (eds) Geochemistry of the Earth Surface and Processes of Mineral Formation. Consejo Sup Invest Gient - CNRS,Madrid, 221–229.

Paradis, S., Hannigan, P., and Dewing, K. (2007). Mississippi Valley-type lead-zinc deposits. In W.D. Goodfellow, Ed., Mineral Deposits of Canada: A synthesis of major deposit-types, district metallogeny, the evolution of geological provinces, and exploration methods, 185–203. Geological Association of Canada, Mineral Deposits Division, Special Publication No. 5, St. John's, Newfoundland.

Partridge, T.C., and Maud, R.R. (1987). Geomorphic evolution of southern Africa since the Mesozoic. South African Journal of Geology, 90, 179–208.

Pascua, C.S., Ohnuma, M., Matsushita, Y., Tamura, K., Yamada, H., Cuadros, J., and Ye, J. (2010). Synthesis of monodisperse Zn-smectite. Applied Clay Sciences, 48(1-2), 55-59. https://doi.org/10.1016/j.clay.2009.12.016

Petit, S., Righi, D., and Decarreau, A. (2008). Transformation of synthetic Zn-stevensite to Zn-talc induced by the Hofmann-Klemen effect. Clays and Clay Minerals, 56(6), 645-654. https://doi.org/10.1346/CCMN.2008.0560605

Rule, A.C., and Radke, R. (1988). "Baileychlore, the Zn end member of the trioctahedral chlorite series," American Mineralogist, 73, 135–139.

Schingaro, E., Ventruti, G., Vinci, D., Balassone, G., Mondillo, N., Nieto, F., Lacalamita M., and Leoni, M. (2021). New insights into the crystal chemistry of sauconite (Zn-smectite) from the Skorpion

826 zinc deposit (Namibia) via a multi-methodological approach. American Mineralogist, 106(2), 290-300.
827 https://doi.org/10.2138/am-2020-7460

828 Schwartz, M.O., Kwok, Y.Y., Davis, D.W., and Akangyang, P. (1996). Geology, geochronology and
829 regional correlation of the Ghanzi Ridge, Botswana. South African Journal of Geology, 99, 245–250.

830 Sharygin, V.V. (2015). Zincian micas from peralkaline phonolites of the Oktyabrsky massif, Azov Sea
831 region, Ukrainian Shield. European Journal of Mineralogy, 27(4), 521-533.
832 https://doi.org/10.1127/ejm/2015/0027-2460

833 Sillitoe, R.H. (2009). Supergene silver enrichment reassessed. In Supergene environments, processes,
834 and products. Society of Economic Geologist Special Publications, 14, 15–32.

835 Singletary, S.J., Hanson, R.E., Martin, M.W., Crowley, J.L., Bowring, S.A., Key, R.M., Ramokate,
836 L.V., Direng, B.B., and Krol, M.A. (2003). Geochronology of basement rocks in the Kalahari Desert,
837 Botswana, and implications for regional Proterozoic tectonics. Precambrian Research, 121, 47–71.
838 https://doi.org/10.1016/S0301-9268(02)00201-2

839 Smith, J.T. (1985). A mineralized solution collapse Breccia Red Dome, Mungana, North Queensland
840 (Doctoral dissertation, B. Sc. thesis, James Cook University, Townsville).

841 Tiller, K.G., and Pickering, J.G. (1974). The synthesis of zinc silicates at 20 C and atmospheric
842 pressure. Clays and Clay Minerals, 22(5-6), 409-416.

843 Torrey, C.E. (1986). Geology and mineralisation of the Red Dome (Mungana) gold skarn deposit, north
844 Queensland, Australia (Vol. 21). Geology Department, James Cook University of North Queensland.

845 Van der Wateren, F.M., and Dunai, T.G. (2001). Late Neogene passive margin denudation history—
846 Cosmogenic isotope measurements from the central Namib desert. Global and Planetary Change, 30,
847 271–307. https://doi.org/10.1016/S0921-8181(01)00104-7

848 Vázquez, M., Nieto, F., Morata, D., Droguet, B., Cariili-Rosua, F.J., and Morales, S. (2014). Evolution
849 of clay mineral assemblages in the Tinguiririca geothermal field, Andean Cordillera of central Chile: an
850 XRD and HRTEM-AEM study. Journal of Volcanology and Geothermal Research, 282, 43-59.
851 https://doi.org/10.1016/j.jvolgeores.2014.05.022

Wendorff, M. (2005). Outline of lithostratigraphy sedimentation and tectonics of the Tsodilo Hills Group, Neoproterozoic Lower Paleozoic siliciclastic succession in NW Botswana. Annales Societatis Geologorum Poloniae, 75, 17–25.

Whitney, D.L., and Evans, B.W. (2010). Abbreviations for names of rock-forming minerals. American Mineralogist, 95, 185–187. https://doi.org/10.2138/am.2010.3371

This is the peer-reviewed, final accepted version for American Mineralogist, published by the Mineralogical Society of America.
The published version is subject to change. Cite as Authors (Year) Title. American Mineralogist, in press.
DOI: https://doi.org/10.2138/am-2022-8439. http://www.minsocam.org/

Figure captions

Figure 1. a) Simplified geological map showing the tectonic framework of Precambrian terranes occurring in Southern Africa (modified after Hanson 2003). Abbreviations: OML = Otavi Mountain land; ZB = Zambezi Belt; IB = Irumide Belt; M = Matchless Belt; **b)** Subsurface geological framework of NW Botswana with the location of the Kihabe and Nxuu prospects (modified after Key and Ayers 2000).

Figure 2. a) XRD patterns of quartzwacke (sample K206) and calcrete (sample K204) host rocks; **b)** XRD patterns of the oriented clay aggregates of the vanadate facies (sample NX414); **c)** Randomly oriented XRD patterns of the vanadate facies (sample NX414) showing the typical hkl peaks of muscovite polytypes. Blue labels indicate the typical peaks of the 1*M* polytype, while the red labels indicate the $2M_1$ polytype. Abbreviations: sme = smectite; mc = mica; TO = serpentine-kaolinite group clay; qz = quartz; cc = calcite; rt = rutile; ms = muscovite.

Figure 3. a) to **c)** XRD patterns of low Zn-clay facies (sample NX504): **a)** and **b)** XRD patterns of the oriented clay aggregates; **c)** Randomly oriented XRD patterns; **d)** to **e)** XRD patterns of the Zn-clay facies (sample NX685): **d)** XRD patterns of the oriented clay aggregates; **e)** Air dried and ethylene glycol pattern showing the shift of *d*-spacing of the 00l and 002 reflections of the 7 Å clay; **f)** Randomly oriented pattern of clays fraction showing the 060 peaks of the phyllosilicates suite. Abbreviations: sme = smectite; I/S = illite-smectite; TO = kaolinite-serpentine group clay; mc = mica; Kfs = K-feldspar; ilt = illite; ght = goethite; TO/sme = 7 Å clay – smectite.

Figure 4. a) and **b)** Optical microscopy (OM) photomicrograph (N+) showing the features of the quartzwacke (sample K206); **c)** and **d)** OM photomicrograph (N+) showing the features of calcrete (sample K204); **e)** OM photomicrograph (N+) showing zoned vanadates cementing recrystallized quartz in the quartzwacke (sample NX504); **f)** BSE photomicrograph showing the association between vanadates and Pb-bearing calcite (sample NX413); **g)** OM photomicrograph (N =) showing the association between rhombohedral Zn-dolomite and vanadates (sample NX685); **h)** BSE photomicrograph of pan-shaped Zn-bearing mica packets associated with vanadinite and Fe-oxy-hydroxides (sample NX413); **i)** OM photomicrograph (N+) showing altered K-feldspars and quartz

902 embedded in a smectite and fine-grained mica matrix (sample NX504); **j)** BSE photomicrograph
903 showing a K-feldspar porphyroblast partially altered by Zn-bearing smectite (sample NX504); **k)** BSE
904 photomicrograph showing Zn-bearing smectite pseudomorph after a K-feldspar porphyroblast. The
905 yellow dashed line indicates the former border of the porphyroblast (sample NX504); **l)** BSE
906 photomicrograph showing mica packets partially altered by Zn-bearing smectite (sample NX504); **m)**
907 OM photomicrograph (N+) showing the textures of the Zn-clay facies (sample NX685); **n)**, **o)** and **p)**
908 BSE photomicrograph showing the textures of authigenic, replacive and massive fraipontite (sample
909 NX685). Abbreviations: Fe-ox = Fe-oxy-hydroxide; qz = quartz; Kfs = K-feldspar; cc = calcite; van =
910 undifferentiated vanadate; vn = vanadinite; des = descloizite; mc = mica; sme = smectite; fr =
911 fraipontite.

912 **Figure 5.** TEM-HRTEM analyses of discrete fraipontite: **a)** large scale STEM-EDX mapping showing
913 the association between muscovite and fraipontite (sample K25); **b)** textural image and SAED pattern
914 of muscovite (1*M* polytype) and fraipontite occurring in the area in the yellow frame in a) (sample
915 K25); **c)** Al vs. K vs. Zn STEM-EDX mapping of the area in the yellow frame in a) highlighting the
916 paragenetic association between fraipontite, kaolinite and muscovite (sample K25); **d)** Al vs. K vs. Zn
917 STEM-EDX mapping of site of interested displaying epitaxial growth relationships between different
918 clay species (sample K26); **e)** textural image of compact clay packages surrounding a partially
919 dissolved willemite grain (sample K26); **f)** HRTEM image of fraipontite showing a double-layer
920 periodicity (sample K26). Abbreviations: ms = muscovite; fr = fraipontite; kln = kaolinite; Fe-ox = Fe-
921 oxy-hydroxide.

922 **Figure 6:** TEM-HRTEM analyses of interstratified fraipontite: **a)** large scale STEM-EDX map of a
923 mineral assemblage (sample K25); **b)** and **c)** K vs. Zn and Ca STEM-EDX maps of the area in the
924 black frame in a) (sample K25), showing the association of muscovite and fraipontite. Abbreviations =
925 fr = fraipontite; qz = quartz; ms = muscovite.

926 **Figure 7.** TEM-HRTEM analyses of interstratified fraipontite: **a)** HAADF textural image of fraipontite
927 packages replacing a K-feldspar detrital grain (sample K25); **b)** STEM-EDX K vs. Zn map of the area
928 of interest shown in a) (sample K25); **c)** and **d)** HRTEM and STEM-EDX Mg vs. Zn map of fraipontite
929 – smectite mixed layer (see inset in b for site location) (sample K25); **e)** and **f)** Mg vs. K vs. Zn and Ca

STEM-EDX maps of a fraipontite – smectite mixed layer replacement after K-feldspar (sample K25). Abbreviations: Kfs = K-feldspar; fr = fraipontite.

Figure 8. TEM-HRTEM analyses of sauconite: **a)** textural image showing wavy smectite packets replacing a K-feldspar grain (sample K21); **b)** SAED pattern showing the basal reflection (00l) of collapsed smectite and of 2-layer muscovite (2*M* polytype) (sample K21); **c)** Fe vs. K vs. Zn STEM-EDX map highlighting the relationship between sauconite and Zn-poor smectite (beidellite) (sample K21); **d)** textural image of smectite packets replacing a detrital K-feldspar (sample K26); **e)** HRTEM image of a partially collapsed smectite (sample K26); **f)** K vs. Zn STEM-EDX map of the area shown in d) (sample K26). Abbreviations: sau = sauconite; Kfs = K-feldspar; bei = beidellite.

Figure 9. TEM-HRTEM analyses of Zn-bearing dioctahedral smectite: **a)** and **b)** textural and Al vs. Zn vs. K STEM-EDX maps showing the paragenetic association between beidellite, kaolinite and muscovite (sample NX685); **c)** SAED pattern of partially collapsed smectite highlighting the 12.6 Å reflection (00l) in the c* direction and the 4.5 Å (02;11) reflection in the a* direction (sample NX685); **d)** HRTEM image showing the kaolinite lattice fringes with a 7 Å periodicity (sample NX685); **e)** HAADF textural image (sample NX685); **f)** SAED pattern showing a the 7 Å periodicity (00l) of kaolinite (sample NX685); **g)** and **h)** K vs. Zn and K vs. Al STEM-EDX chemical maps showing the spatial relationship between kaolinite, Zn-bearing beidellite and muscovite (sample NX685). Abbreviations: ms = muscovite; bei = beidellite; kln = kaolinite.

Figure 10. TEM-HRTEM analyses of the beidellite-fraipontite association: **a)** HAADF textural image showing the association between Zn-rich (bright white) and Zn-poor (pale white) clay minerals (sample NX685); **b)** HRTEM image showing the fraipontite lattice fringes with a 7 Å periodicity (sample NX685); **c)** Al vs. Zn STEM-EDX map of the area shown in a) (sample NX685); **d)** textural image showing the relationship between detrital mica and newly formed clay packets (sample K25); **e)** SAED pattern showing the typical reflections of collapsed smectite (00l = 9.2 Å), fraipontite (00l = 7 Å) and of 2*M* muscovite polytype (00l = 20 Å) (sample K25); **f)** Fe vs. Zn STEM-EDX map of inset area in d) showing the relationship between fraipontite and Zn-poor dioctahedral smectite; **g)** HAADF image of fraipontite epitaxial overgrown onto beidellite (sample K25); **h)** and **i)** STEM-EDX spectra of fraipontite and Zn-bearing beidellite, respectively (sample K25).

This is the peer-reviewed, final accepted version for American Mineralogist, published by the Mineralogical Society of America.
The published version is subject to change. Cite as Authors (Year) Title. American Mineralogist, in press.
DOI: https://doi.org/10.2138/am-2022-8439. http://www.minsocam.org/

Figure 11. TEM-HRTEM analyses of the clay assemblage in the sulfide facies: **a)** textural image of compact muscovite packets (sample K8); **b)** SAED pattern showing the basal reflection of 1*M* muscovite polytype (sample K8); **c)** HAADF image of muscovite packets in epitaxial relationship with kaolinite (sample K8); **d)** SAED pattern showing the basal reflections of double and single layers (2*M*) muscovite polytypes (sample K8); **e)** STEM-EDX of kaolinite.

Figure 12. Binary plots showing the chemical composition by AEM of clay minerals in the Kihabe-Nxuu prospects.

Figure 13. a) 4Si-M^{+}-$3R^{2+}$ chemiographic diagram. This representation is based on the following three axis: *i.* M^{+}: accounting for the concentration of the interlayer cations; *ii.* $3R2^{+}$: representing the contribution of bivalent cations in the octahedral sheet; *iii.* 4Si: representing the contribution of the tetrahedral sheet. Literature data: black dots represent the nominal composition of hendricksite (H), sauconite (S), muscovite (M), kaolinite (K), fraipontite (F) and beidellite (B); a = Zn-bearing beidellite from the Accha – Yanque district, Peru (Mondillo et al. 2015); b = kaolinite and Zn-bearing dioctahedral smectite (beidellite and montmorillonite) from the Mina Grande and Cristal deposits, Peru (Balassone et al. 2020); c = Zn-illite from the Mina Grande and Cristal zinc deposits, Peru (Balassone et al. 2020); d = muscovite from Skorpion, Namibia (Balassone et al. 2017); e = dioctahedral/trioctahedral Zn-illite from the Mina Grande and Cristal deposits, Peru (Balassone et al. 2020); f = compositional trend between the compositional fields of mica, fraipontite, and sauconite from Bou Arhous, Morocco (Choulet et al. 2016); g = sauconite from the Accha – Yanque district, Peru (Mondillo et al. 2015); h = sauconite from the Mina Grande and Cristal deposits, Peru (Balassone et al. 2020); i = sauconite from Skorpion, Namibia (Balassone et al. 2020); j = fraipontite from the Mina Grande and Cristal deposits, Peru (Balassone et al. 2020).

Figure 14. Summary of the paragenetic relationships between the clay minerals according to the micro- to nanoscale TEM analysis. Notes: * = includes discrete and interstratified fraipontite; ** = Zn^{2+} input from earlier Zn-phases (i.e., willemite and sphalerite).

Table 1: Summary of Zn-bearing phyllosilicates (IMA and ruff data

Group	Mineral	Structural configuration
Smectite (15 Å)	sauconite	trioctahedral
	beidellite	dioctahedral
	montmorillonite	
Kaolinite-serpentine (7 Å)	fraipontite	trioctahedral
Chlorite (14 Å)	baileychlore*	
Mica (10 Å)	muscovite	dioctahedral
	illite*	
	hendricksite	trioctahedral

* = from http://www.webmineral.com.

ıbses).

Ideal formula
$Na_{0.3}Zn_3(Si,Al)_4O_{10}(OH)_2 \cdot 4H_2O$
$(Na,Ca)_{0.3}Al_2(Si,Al)_4O_{10}(OH)_2 \cdot n(H_2O)$
$(Na,Ca)_{0.3}(Al,Mg)_2Si_4O_{10}(OH)_2 \cdot nH_2O$
$(Zn,Al)_3(Si,Al)_2O_5(OH)_4$
$(Zn,Fe^{2+},Al,Mg)_6(Si,Al)_4O_{10}(OH)_8$
$KAl_2(Si_3Al)O_{10}(OH)_2$
$(K,H_3O)(Al,Mg,Fe)_2(Si,Al)_4O_{10}[(OH)_2,(H_2O)]$
$KZn_3(Si_3Al)O_{10}(OH)_2$

Table 2: Provenance and mineralogical composition (XRPD) of the studied samples from the Kihabe and

Deposit	Borehole ID	Sample ID	Depth (m)	Facies	van	des
		NX969	5.00 - 6.00	mixed calcrete - vanadates		
	NXDD0030	NX971	7.00 - 7.45	mixed calcrete - vanadates		X
		NX972	7.45 - 8.00	vanadate		
	NXDD0033	NX341	52.46 - 53.00	vanadate		
Nxuu	NXDD0039	NX685	51.00 - 51.62	mixed vanadate - Zn clay		X
		NX413	31.00 - 31.50	vanadate		X
	NXDD0040	NX414	31.50 - 32.00	vanadate	X	
		NX415	32.00 - 32.61	vanadate	X	X
	NXDD0045	NX504	41.00 - 41.36	mixed vanadate - low zn clay		X
	KDD125	K8**	57.08 - 58.57	sulphide		
	KDD143	K21	51.24 - 51.60	Zn clay		
	KDD143	K23	51.86 - 52.20	Zn clay		
	KDD143	K25	52.55 - 52.72	Zn clay		
Kihabe	KDD143	K26	52.72 - 53.00	Zn clay		
	KDD203	K203	22.00 - 23.00	Zn clay		
	KDD204	K204	19.00 - 20.00	calcrete		X
	KDD206	K206	63.00 - 67.00	Zn clay		

Abbreviations are from Whitney and Evans (2010). Notes: * = kaolinite - serpentine group clays: ** = dat

Nxuu prospects.

Mineralogy by XRPD on whole-rock specimens and on clay aggregates

sme	kln - srp*	chl	qz	ms - ilt	cal	dol	kfs	gth	sm	sp
X	X		X	X	X					
X	X		X	X	X					
X	X		X	X	X					
X	X	X	X	X	X	X		X		
X	X		X	X	X			X		
X	X		X	X	X			X		
			X	X						
			X	X						
X	X		X	X						
			X	X					X	X
			X	X			X			
			X	X			X			
X			X	X			X			
X			X	X			X			
X	X		X	X				X		
X	X		X	X	X					
X	X		X	X	X			X		

:a from Mondillo et al. (2020).

gn	hem
X	X

Table 3: Selected structural formulae (apfu) of trioctahedral clay species obtained by AEM.

Reference	Average (n = 62)	St. dev.	Nxuu	Kihabe
Sample ID	N/A	N/A	NX685	K25
Mineral			Fraipontite	
Si	1.74	0.18	2.06	1.93
Al^{IV}	0.27	0.16	-	0.07
Σ_{tet}	2.01	0.04	2.06	2.00
Ti	-	0.00	-	-
Mg	0.18	0.11	0.14	0.61
Fe^{a}	0.05	0.04	0.10	0.03
Zn	2.09	0.37	1.43	1.37
Mn	-	0.00	-	-
Al^{VI}	0.63	0.28	1.16	0.94
$\sum_{oct}$	2.95	0.05	2.84	2.95
Ca	0.02	0.02	0.08	0.01
Na	-	0.00	-	-
K	0.01	0.02	0.01	0.04
$\sum_{int}$	0.04	0.03	0.10	0.05
Zn/Al_{tot}	2.47	0.86	1.23	1.36
Si/Al_{tot}	1.99	0.43	1.78	1.90

Notes: N/A = not applicable; - = not detected; a = Fe was considered in its bivalent state for trioctah

Average (n = 24)	St. dev.	Nxuu	Kihabe
N/A	N/A	NX685	K26
		Sauconite	
3.64	0.25	3.14	3.64
0.36	0.25	0.86	0.36
4.00	0.01	4.00	4.00
-	0.00	-	-
0.14	0.07	0.23	0.10
0.07	0.04	0.14	0.02
2.64	0.28	2.07	3.13
-	0.00	-	-
0.31	0.23	0.70	0.03
3.15	0.09	3.14	3.28
0.10	0.05	0.12	0.02
-	0.00	-	-
0.05	0.08	0.04	-
0.15	0.09	0.16	0.02
4.53	1.60	1.33	7.98
6.19	1.95	2.01	9.26

ıedral species

Table 4: Selected structural formulae (apfu) of dioctahedral clay species obtained by AEM.

Reference	Average (n = 17)	St. dev.	Kihabe	Nxuu
Sample ID	N/A	N/A	K25	NX685
Mineral			Beidellite	
Si	3.49	0.34	2.89	3.91
Al^{IV}	0.51	0.34	1.11	0.09
∑tet	4.00	0.00	4.00	4.00
Ti	-	0.00	-	-
Mg	0.17	0.10	0.15	0.32
Fe^{a}	0.15	0.17	0.01	0.05
Zn	0.34	0.22	0.58	0.17
Mn	-	0.00	-	-
Al^{VI}	1.51	0.40	1.54	1.61
$\sum_{oct}$	2.17	0.09	2.28	2.16
Ca	0.06	0.05	-	0.13
Na	-	0.00	-	-
K	0.07	0.08	0.02	0.01
∑int	0.13	0.09	0.02	0.14
Zn/Al_{tot}	0.18	0.14	0.22	0.10
Si/Al_{tot}	1.83	0.51	1.09	2.31

Notes: N/A = not applicable; - = not detected; a = Fe was considered in its trivalent state for dioctah

Average (n = 11)	St. dev.	Kihabe	Nxuu	Average (n = 3)
N/A	N/A	K25	NX685	N/A
Mica*		Muscovite	Illite	
3.11	0.08	3.13	3.24	1.93
0.89	0.08	0.87	0.76	0.07
4.00	0.00	4.00	4.00	2.00
0.01	0.02	0.03	-	-
0.18	0.04	0.16	0.17	0.01
0.03	0.01	0.03	0.04	0.01
0.11	0.21	0.29	0.09	0.04
0.00	0.00	0.00	-	-
1.78	0.13	1.55	1.81	1.93
2.11	0.12	2.07	2.11	1.99
0.01	0.01	0.02	0.04	0.01
0.00	0.00	0.00	-	-
0.83	0.22	1.06	0.66	-
0.84	0.22	1.08	0.70	0.01
2.06	0.09	0.12	0.04	0.02
1.06	0.07	1.29	1.26	0.97

ıedral species; * avegare composition considering both muscovite- and illite-like compositions.

St. dev.	Kihabe	Nxuu
N/A	K26	NX685
	Kaolinite	
0.05	1.96	1.87
0.05	0.04	0.13
0.00	2.00	2.00
0.00	-	-
0.02	-	0.03
0.00	0.01	0.01
0.03	-	0.04
0.00	-	-
0.05	1.99	1.91
0.01	2.00	1.98
0.00	-	0.01
0.00	-	-
0.01	-	0.01
0.01	-	0.02
0.02	-	0.02
0.05	0.96	0.92

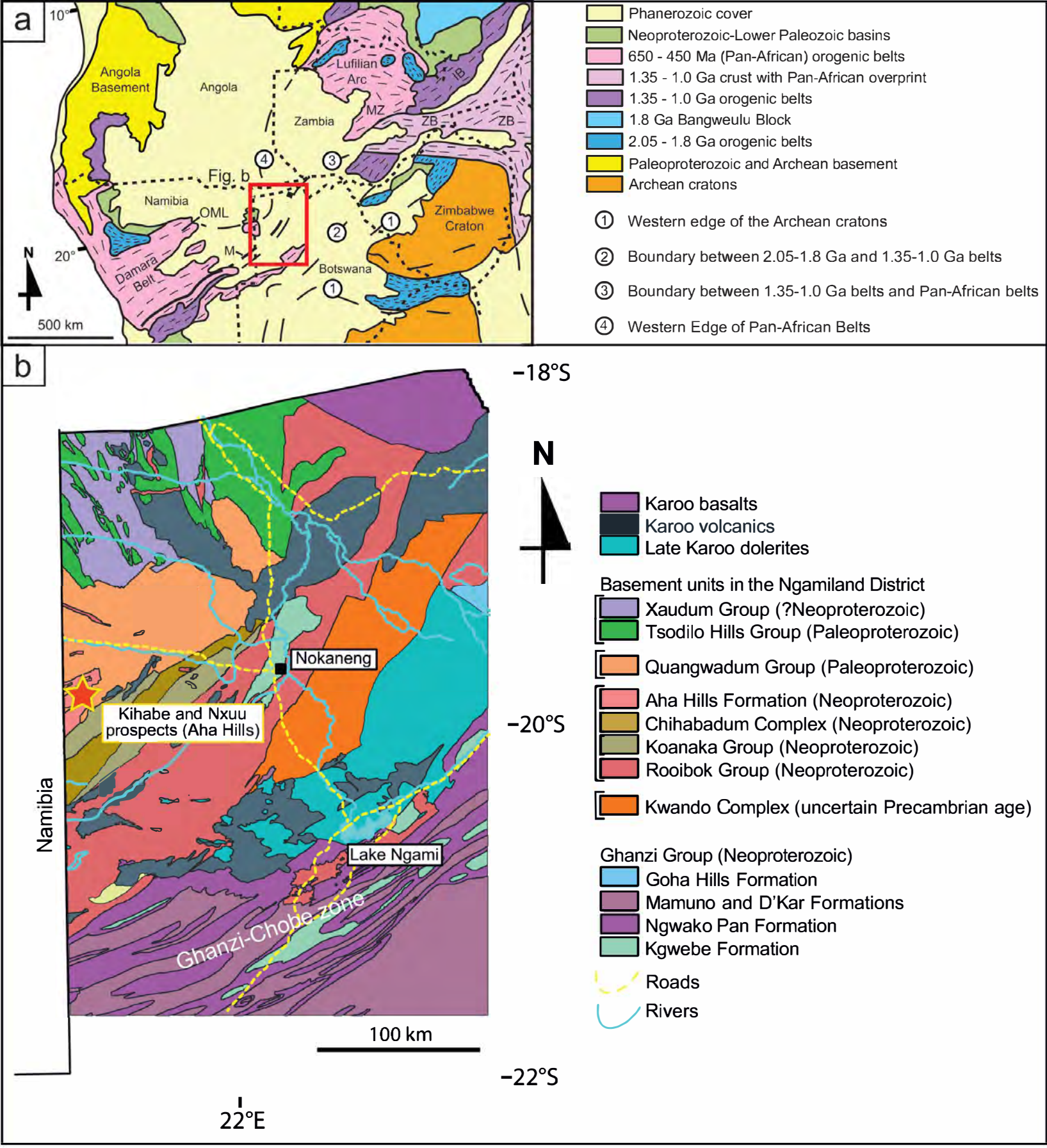
a
10°
Angola Basement
Angola
Lufilian Arc
IB
MZ
Zambia
ZB
ZB
Fig. b
4
3
Namibia
OML
2
1
Zimbabwe Craton
N
20°
M
Damara Belt
Botswana
1
500 km
Phanerozoic cover
Neoproterozoic-Lower Paleozoic basins
650 - 450 Ma (Pan-African) orogenic belts
1.35 - 1.0 Ga crust with Pan-African overprint
1.35 - 1.0 Ga orogenic belts
1.8 Ga Bangweulu Block
2.05 - 1.8 Ga orogenic belts
Paleoproterozoic and Archean basement
Archean cratons
① Western edge of the Archean cratons
② Boundary between 2.05-1.8 Ga and 1.35-1.0 Ga belts
③ Boundary between 1.35-1.0 Ga belts and Pan-African belts
④ Western Edge of Pan-African Belts
b
−18°S
N
Nokaneng
Kihabe and Nxuu prospects (Aha Hills)
−20°S
Namibia
Lake Ngami
Ghanzi-Chobe zone
100 km
−22°S
22°E
Karoo basalts
Karoo volcanics
Late Karoo dolerites
Basement units in the Ngamiland District
Xaudum Group (?Neoproterozoic)
Tsodilo Hills Group (Paleoproterozoic)
Quangwadum Group (Paleoproterozoic)
Aha Hills Formation (Neoproterozoic)
Chihabadum Complex (Neoproterozoic)
Koanaka Group (Neoproterozoic)
Rooibok Group (Neoproterozoic)
Kwando Complex (uncertain Precambrian age)
Ghanzi Group (Neoproterozoic)
Goha Hills Formation
Mamuno and D'Kar Formations
Ngwako Pan Formation
Kgwebe Formation
Roads
Rivers

Fig. 1

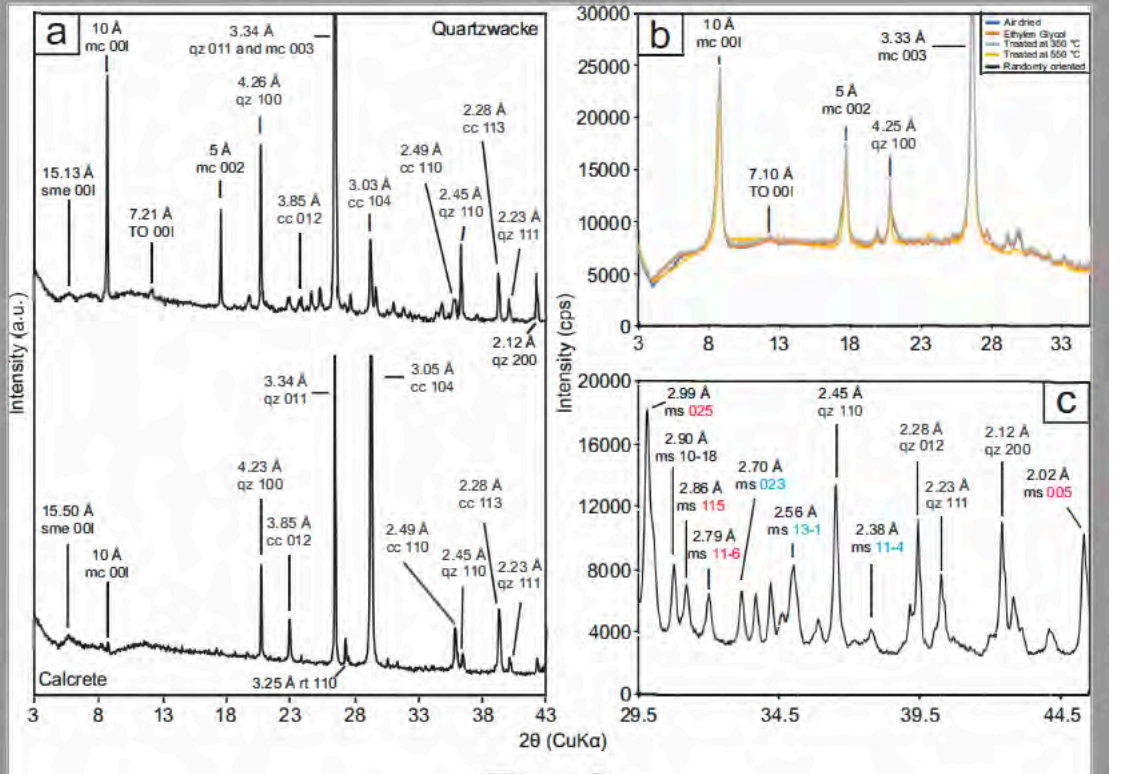
a
Quartzwacke
10 Å
mc 001
3.34 Å
qz 011 and mc 003
4.26 Å
qz 100
5 Å
mc 002
15.13 Å
sme 001
7.21 Å
TO 001
3.85 Å
cc 012
3.03 Å
cc 104
2.49 Å
cc 110
2.45 Å
qz 110
2.28 Å
cc 113
2.23 Å
qz 111
2.12 Å
qz 200
3.34 Å
qz 011
3.05 Å
cc 104
4.23 Å
qz 100
15.50 Å
sme 001
3.85 Å
cc 012
10 Å
mc 001
2.49 Å
cc 110
2.45 Å
qz 110
2.28 Å
cc 113
2.23 Å
qz 111
Calcrete
3.25 Å rt 110
Intensity (a.u.)
3
8
13
18
23
28
33
38
43
2θ (CuKα)
b
10 Å
mc 001
3.33 Å
mc 003
5 Å
mc 002
4.25 Å
qz 100
7.10 Å
TO 001
Air dried
Ethylen Glycol
Treated at 350 °C
Treated at 550 °C
Randomly oriented
Intensity (cps)
30000
25000
20000
15000
10000
5000
0
3
8
13
18
23
28
33
c
2.99 Å
ms 025
2.90 Å
ms 10-18
2.86 Å
ms 115
2.79 Å
ms 11-6
2.70 Å
ms 023
2.56 Å
ms 13-1
2.45 Å
qz 110
2.38 Å
ms 11-4
2.28 Å
qz 012
2.23 Å
qz 111
2.12 Å
qz 200
2.02 Å
ms 005
20000
16000
12000
8000
4000
0
29.5
34.5
39.5
44.5

Fig. 2

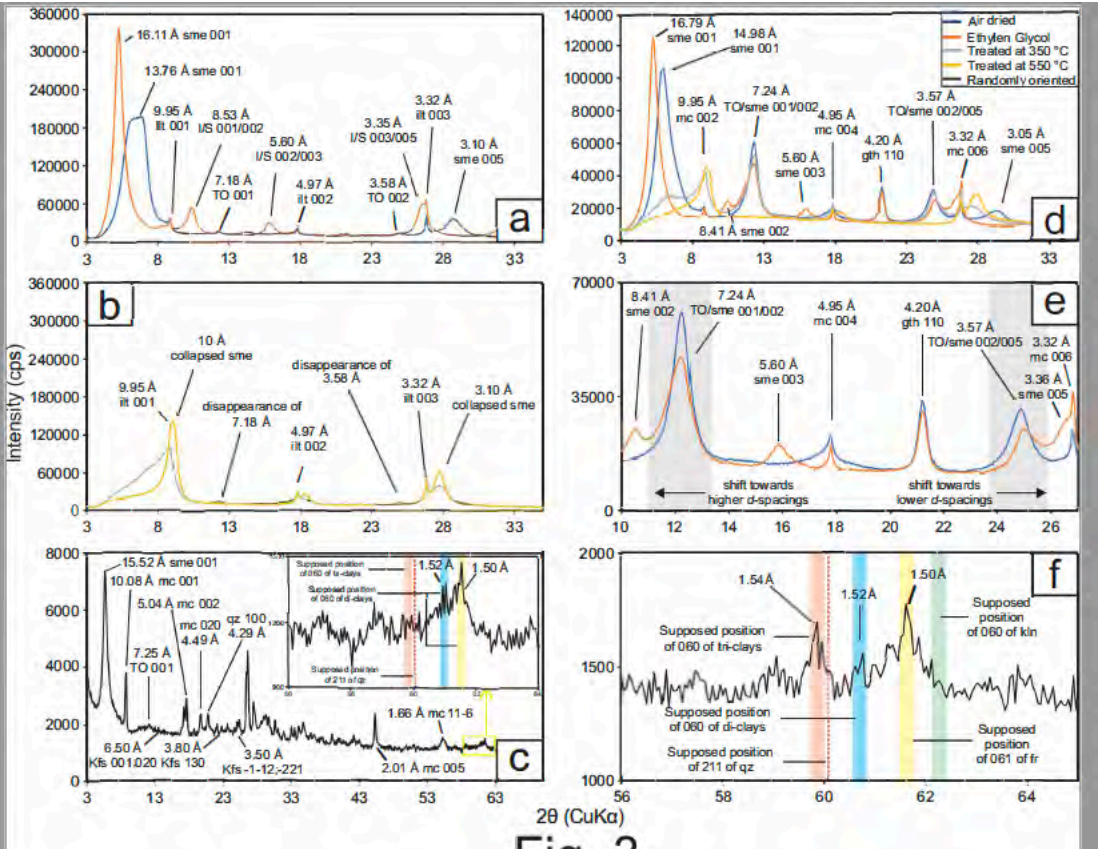
a
16.11 Å sme 001
13.76 Å sme 001
9.95 Å ilt 001
8.53 Å I/S 001/002
5.60 Å I/S 002/003
7.18 Å TO 001
4.97 Å ilt 002
3.58 Å TO 002
3.35 Å I/S 003/005
3.32 Å ilt 003
3.10 Å sme 005
b
10 Å collapsed sme
9.95 Å ilt 001
disappearance of 7.18 Å
4.97 Å ilt 002
disappearance of 3.58 Å
3.32 Å ilt 003
3.10 Å collapsed sme
Intensity (cps)
c
15.52 Å sme 001
10.08 Å mc 001
5.04 Å mc 002
7.25 Å TO 001
mc 020 4.49 Å
qz 100 4.29 Å
6.50 Å Kfs 001/020
3.80 Å Kfs 130
3.50 Å Kfs -1-12,-221
1.66 Å mc 11-6
2.01 Å mc 005
Supposed position of 060 of tri-clays
Supposed position of 060 of di-clays
Supposed position of 211 of qz
1.54 Å
1.52 Å
1.50 Å
d
16.79 Å sme 001
14.98 Å sme 001
9.95 Å mc 002
7.24 Å TO/sme 001/002
4.95 Å mc 004
5.60 Å sme 003
4.20 Å gth 110
3.57 Å TO/sme 002/005
3.32 Å mc 006
3.05 Å sme 005
8.41 Å sme 002
Air dried
Ethylen Glycol
Treated at 350 °C
Treated at 550 °C
Randomly oriented
e
8.41 Å sme 002
7.24 Å TO/sme 001/002
4.95 Å mc 004
4.20 Å gth 110
3.57 Å TO/sme 002/005
3.32 Å mc 006
3.36 Å sme 005
5.60 Å sme 003
shift towards higher d-spacings
shift towards lower d-spacings
f
1.54 Å
1.52 Å
1.50 Å
Supposed position of 060 of tri-clays
Supposed position of 060 of kln
Supposed position of 060 of di-clays
Supposed position of 211 of qz
Supposed position of 061 of fr
2θ (CuKα)

Fig. 3

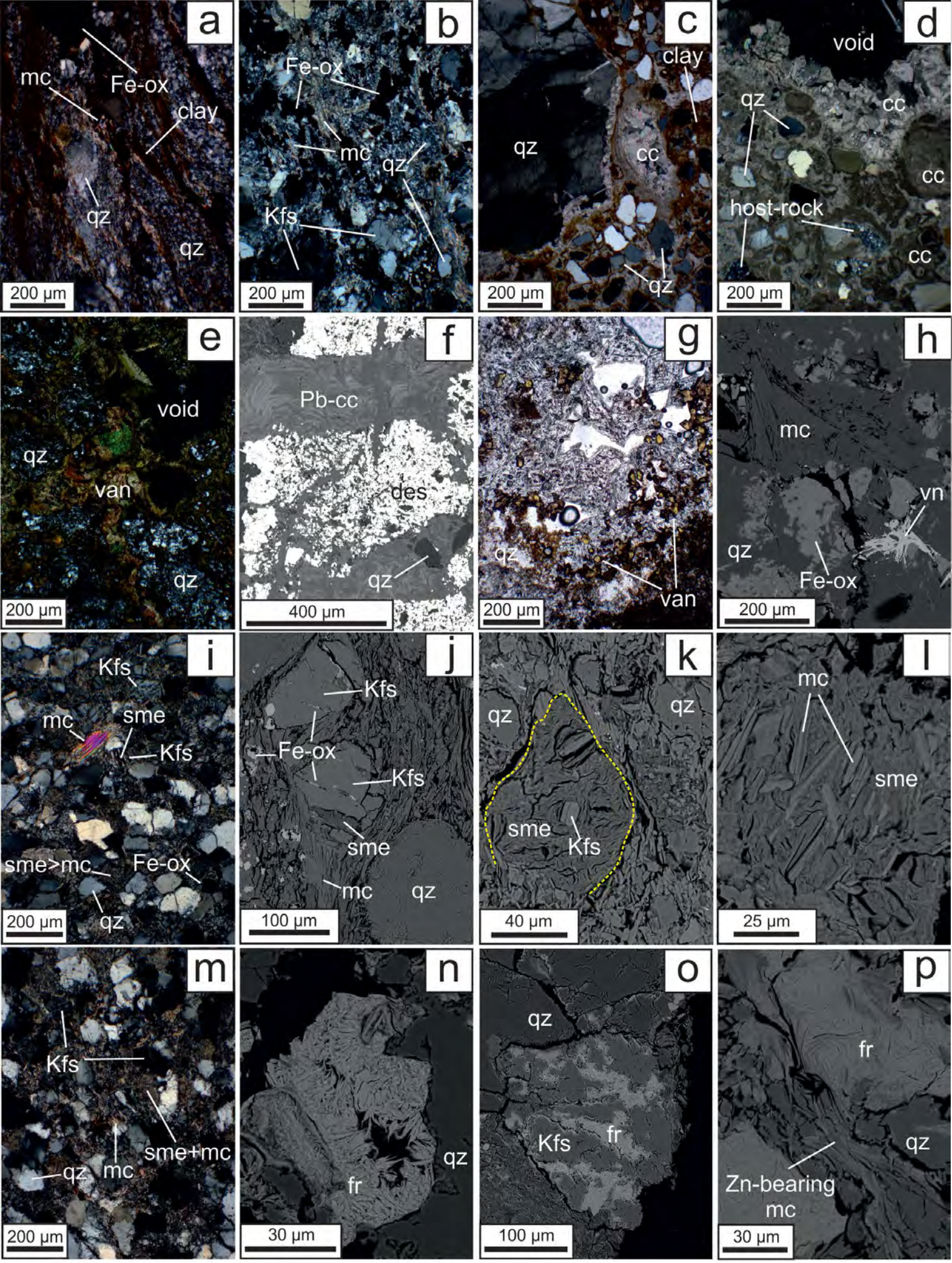
a
mc
Fe-ox
clay
qz
qz
200 µm
b
Fe-ox
mc
qz
Kfs
200 µm
c
clay
qz
cc
qz
200 µm
d
void
qz
cc
cc
host-rock
cc
200 µm
e
void
qz
van
qz
200 µm
f
Pb-cc
des
qz
400 µm
g
qz
van
200 µm
h
mc
vn
qz
Fe-ox
200 µm
i
Kfs
mc
sme
Kfs
sme>mc
Fe-ox
qz
200 µm
j
Kfs
Fe-ox
Kfs
sme
mc
qz
100 µm
k
qz
qz
sme
Kfs
40 µm
l
mc
sme
25 µm
m
Kfs
sme+mc
qz
mc
200 µm
n
qz
fr
30 µm
o
qz
Kfs
fr
100 µm
p
fr
qz
Zn-bearing
mc
30 µm

Fig. 4

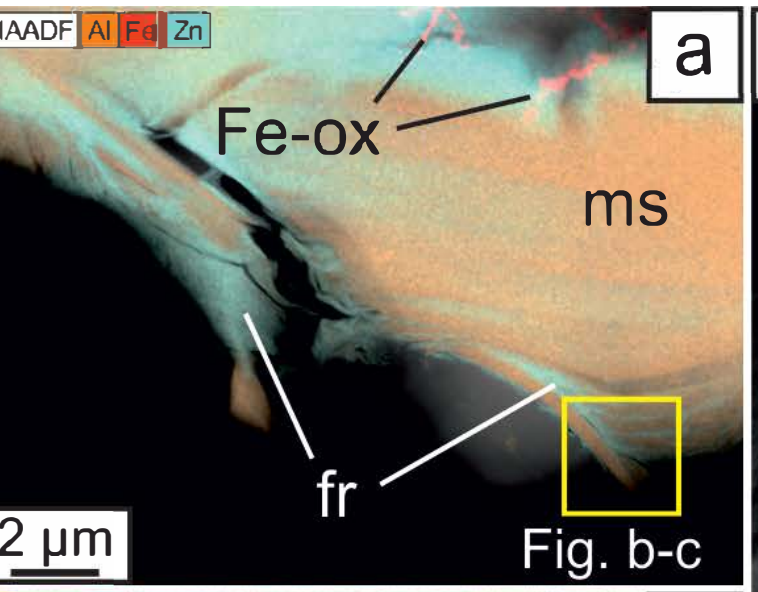
AADF Al Fe Zn
a
Fe-ox
ms
fr
Fig. b-c
2 µm

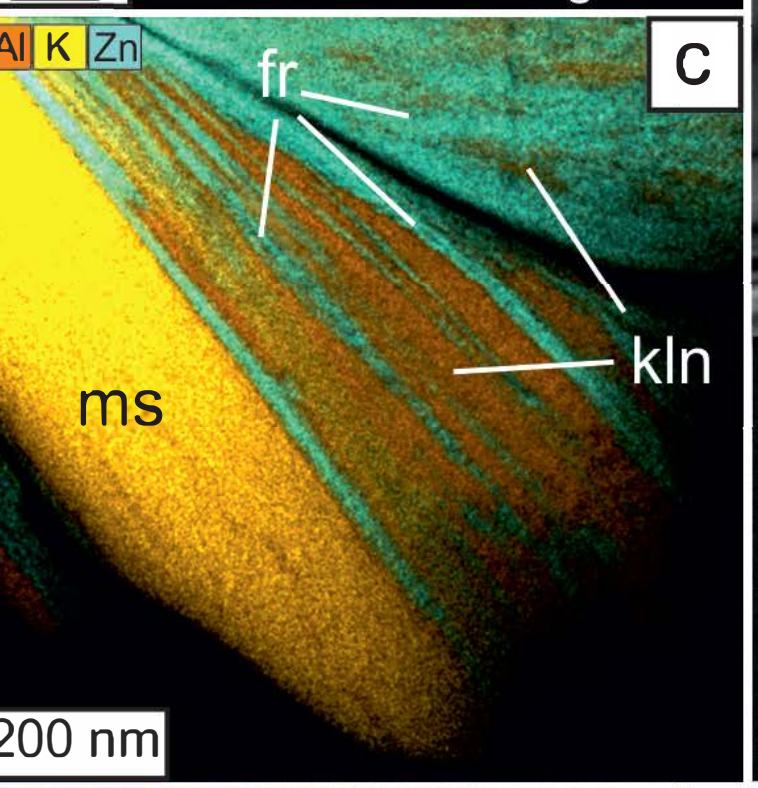
Al K Zn
c
fr
kln
ms
200 nm

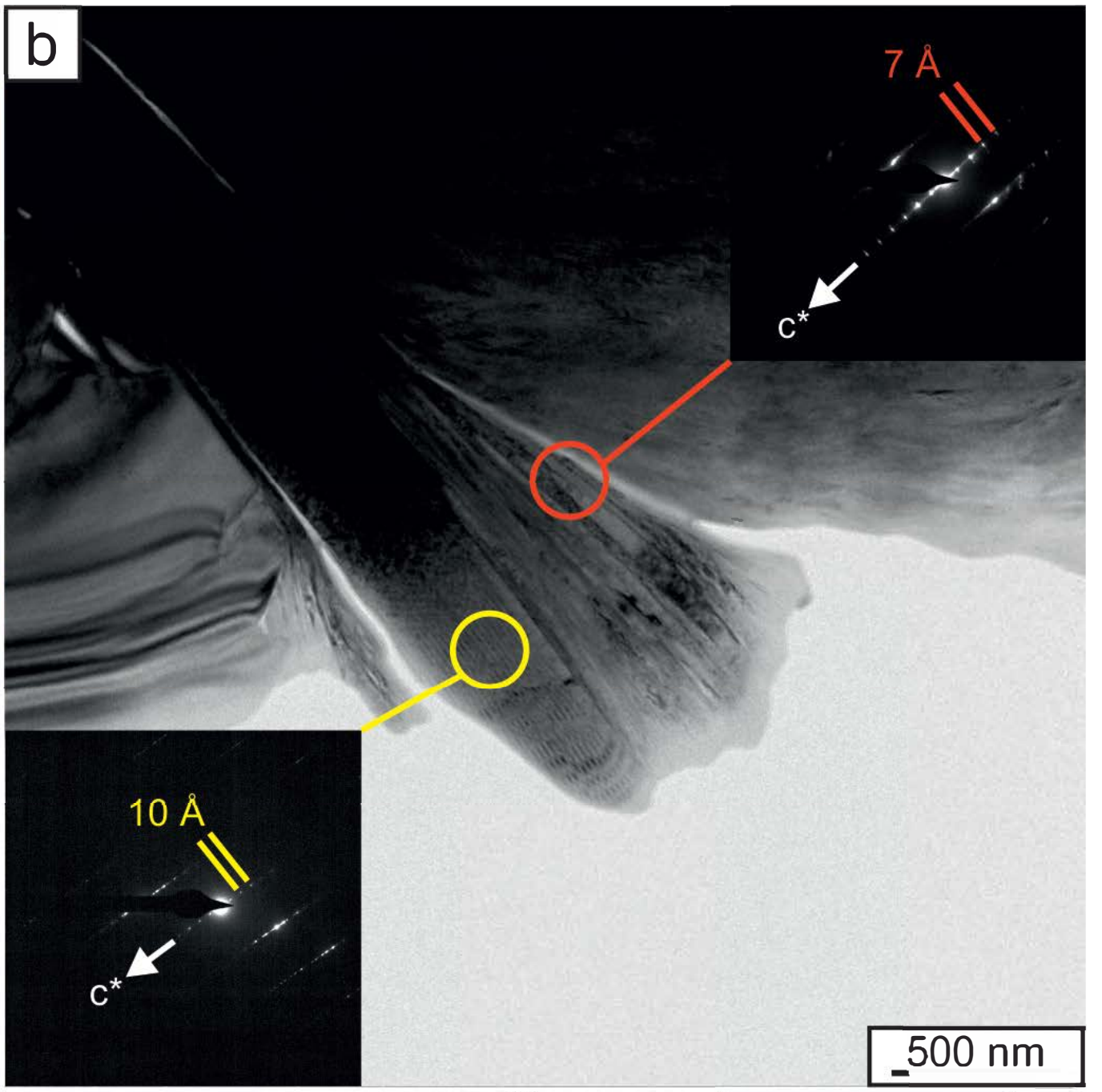
b
7 Å
c*
10 Å
c*
500 nm

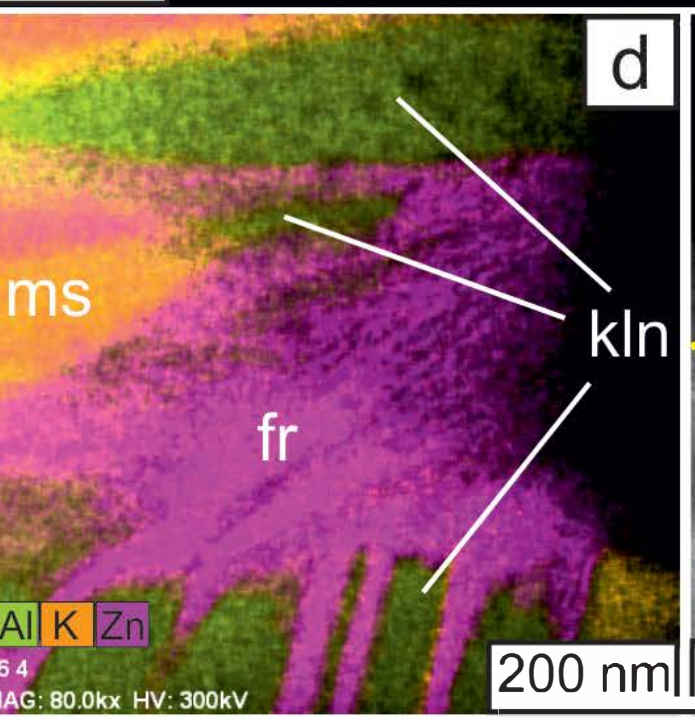
d
ms
kln
fr
Al K Zn
6 4
AG: 80.0kx HV: 300kV
200 nm

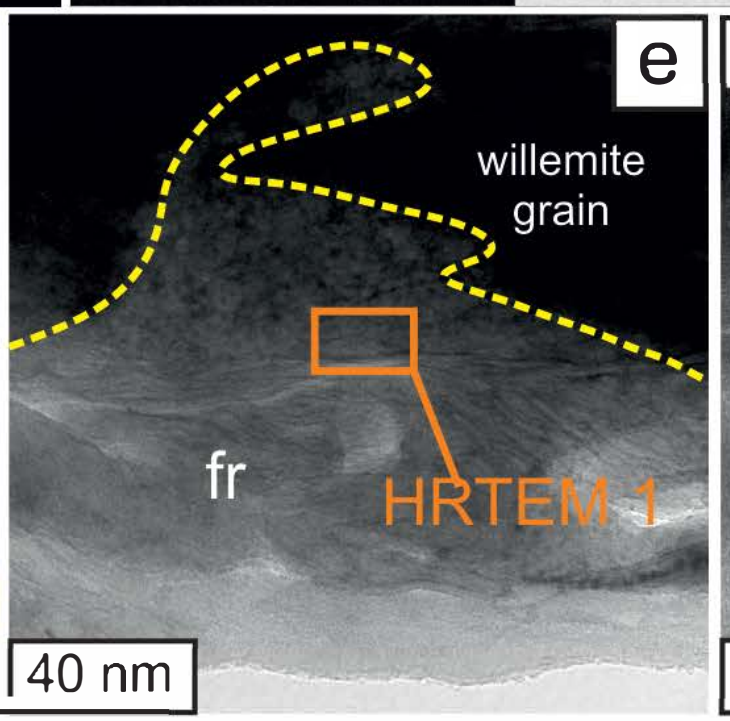
e
willemite
grain
fr
HRTEM 1
40 nm

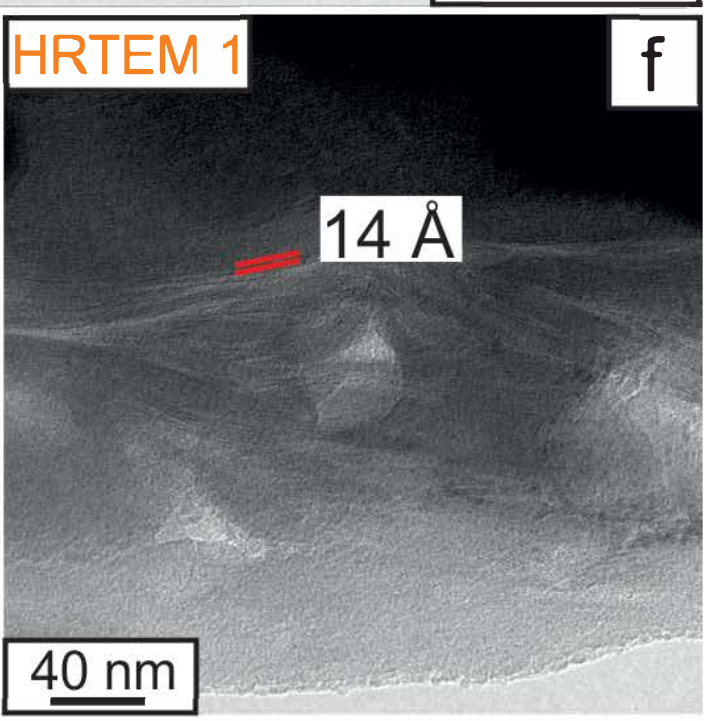
HRTEM 1
f
14 Å
40 nm

Fig. 5

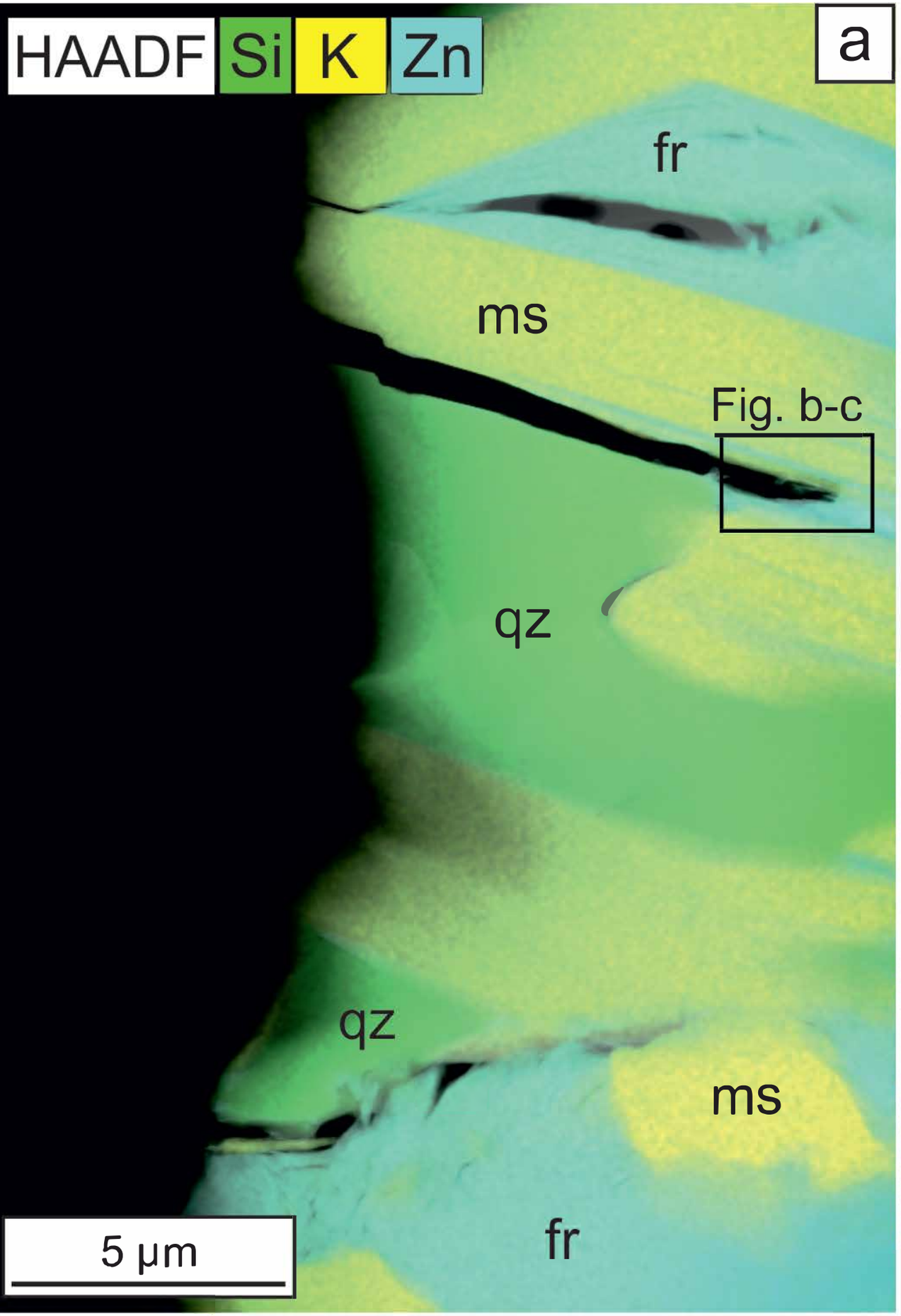
HAADF
Si
K
Zn
a
fr
ms
Fig. b-c
qz
qz
ms
fr
5 µm

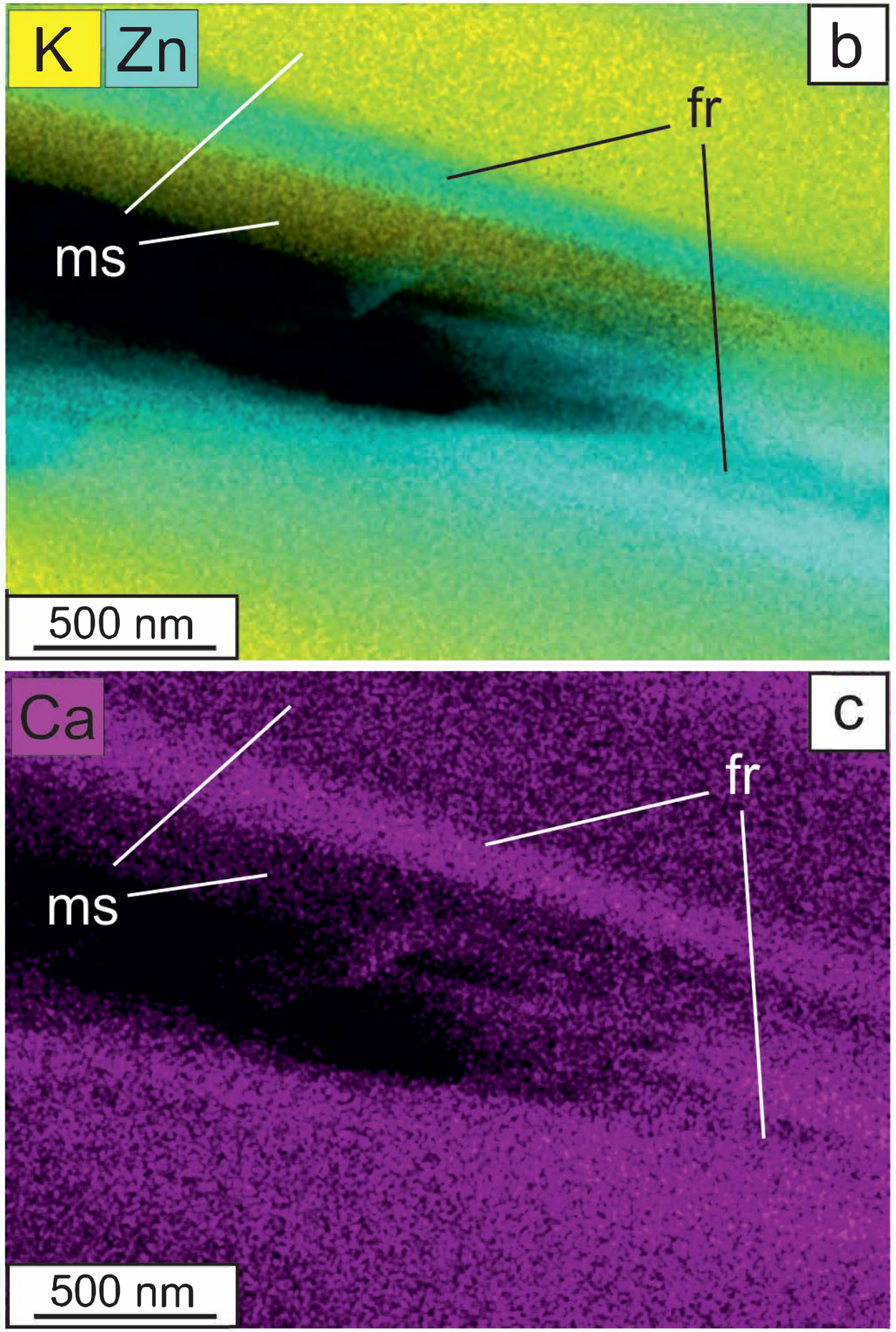
K
Zn
b
fr
ms
500 nm
Ca
c
fr
ms
500 nm

Fig. 6

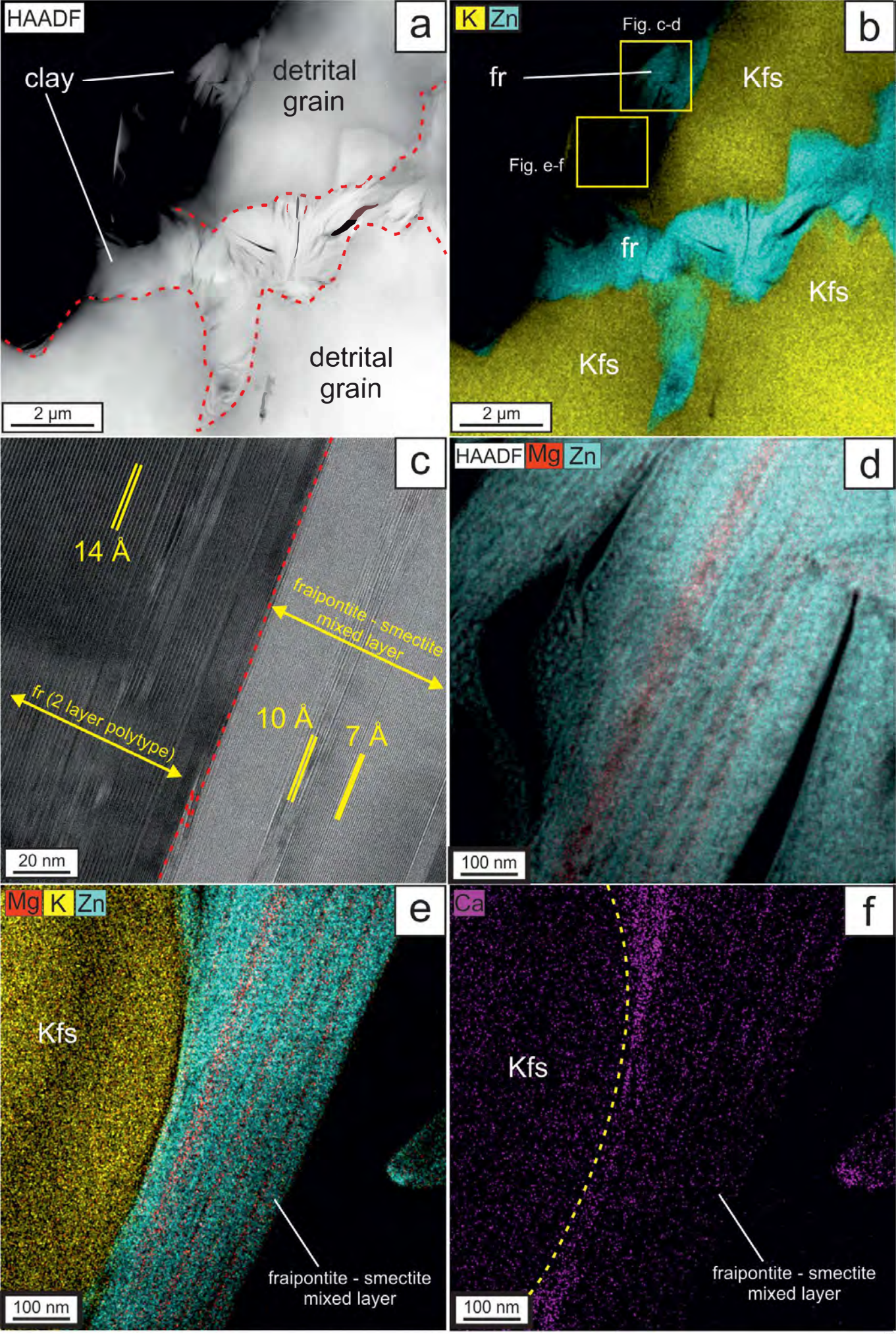
HAADF
a
clay
detrital grain
detrital grain
2 µm
K Zn
b
Fig. c-d
fr
Kfs
Fig. e-f
fr
Kfs
Kfs
2 µm
c
14 Å
fraipontite - smectite mixed layer
fr (2 layer polytype)
10 Å
7 Å
20 nm
HAADF Mg Zn
d
100 nm
Mg K Zn
e
Kfs
fraipontite - smectite mixed layer
100 nm
Ca
f
Kfs
fraipontite - smectite mixed layer
100 nm

Fig. 7

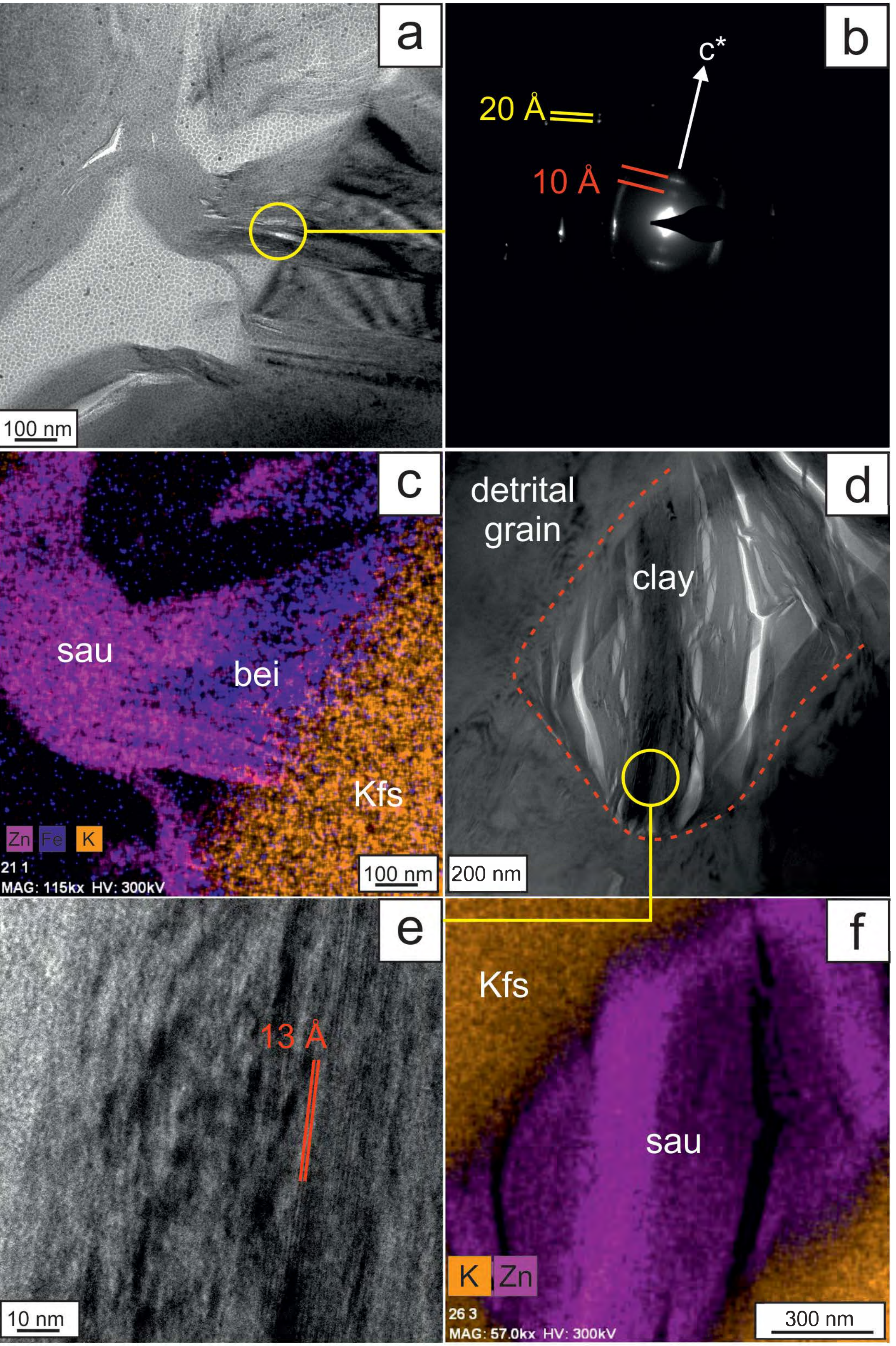
a
100 nm
b
c*
20 Å
10 Å
c
sau
bei
Kfs
Zn
Fe
K
21 1
MAG: 115kx HV: 300kV
100 nm
d
detrital
grain
clay
200 nm
e
13 Å
10 nm
f
Kfs
sau
K
Zn
26 3
MAG: 57.0kx HV: 300kV
300 nm

Fig. 8

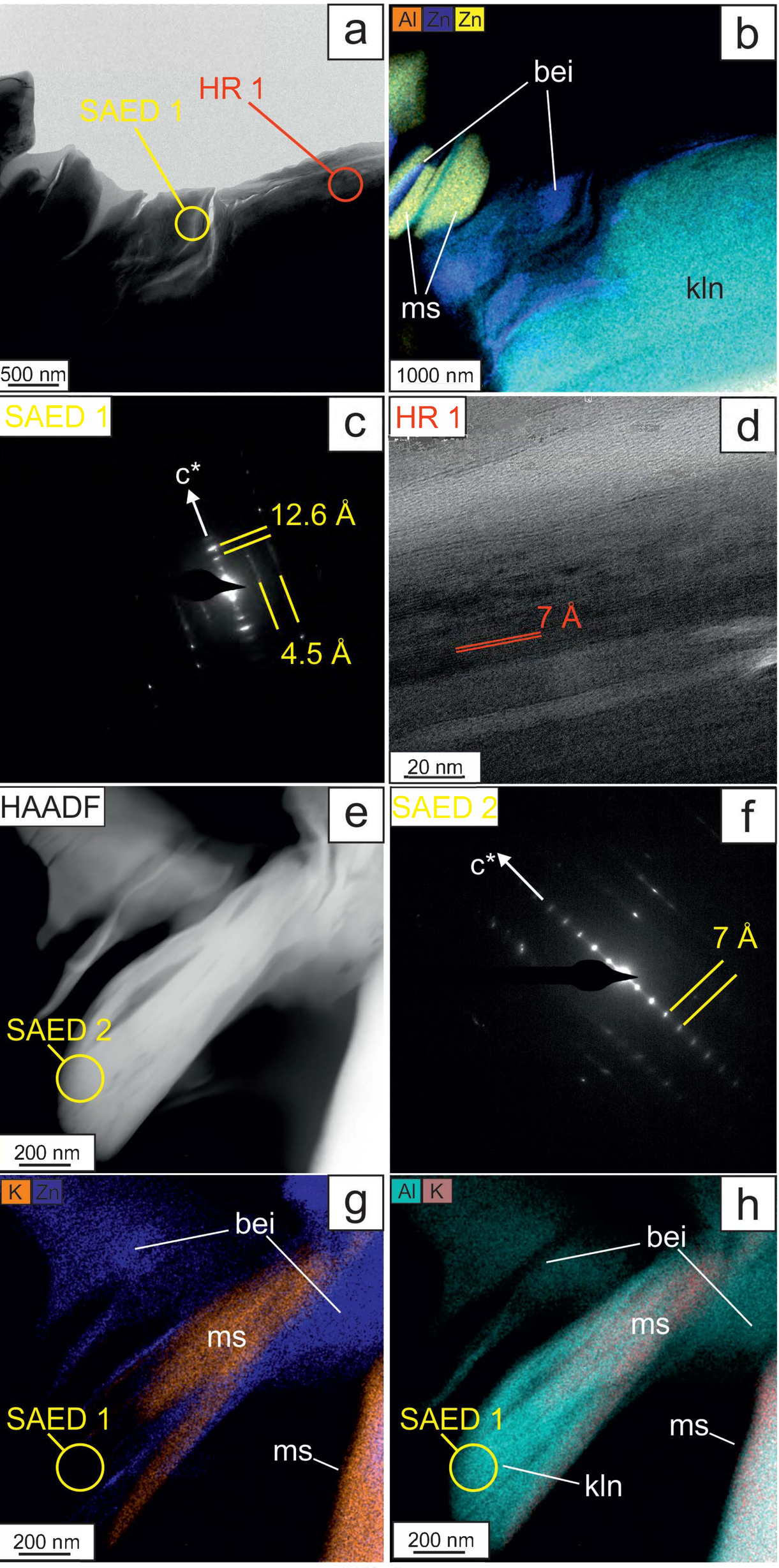
a
HR 1
SAED 1
500 nm
b
Al Zn Zn
bei
ms
kln
1000 nm
SAED 1
c
c*
12.6 Å
4.5 Å
HR 1
d
7 Å
20 nm
HAADF
e
SAED 2
200 nm
SAED 2
f
c*
7 Å
K Zn
g
bei
ms
SAED 1
ms
200 nm
Al K
h
bei
ms
SAED 1
ms
kln
200 nm

Fig. 9

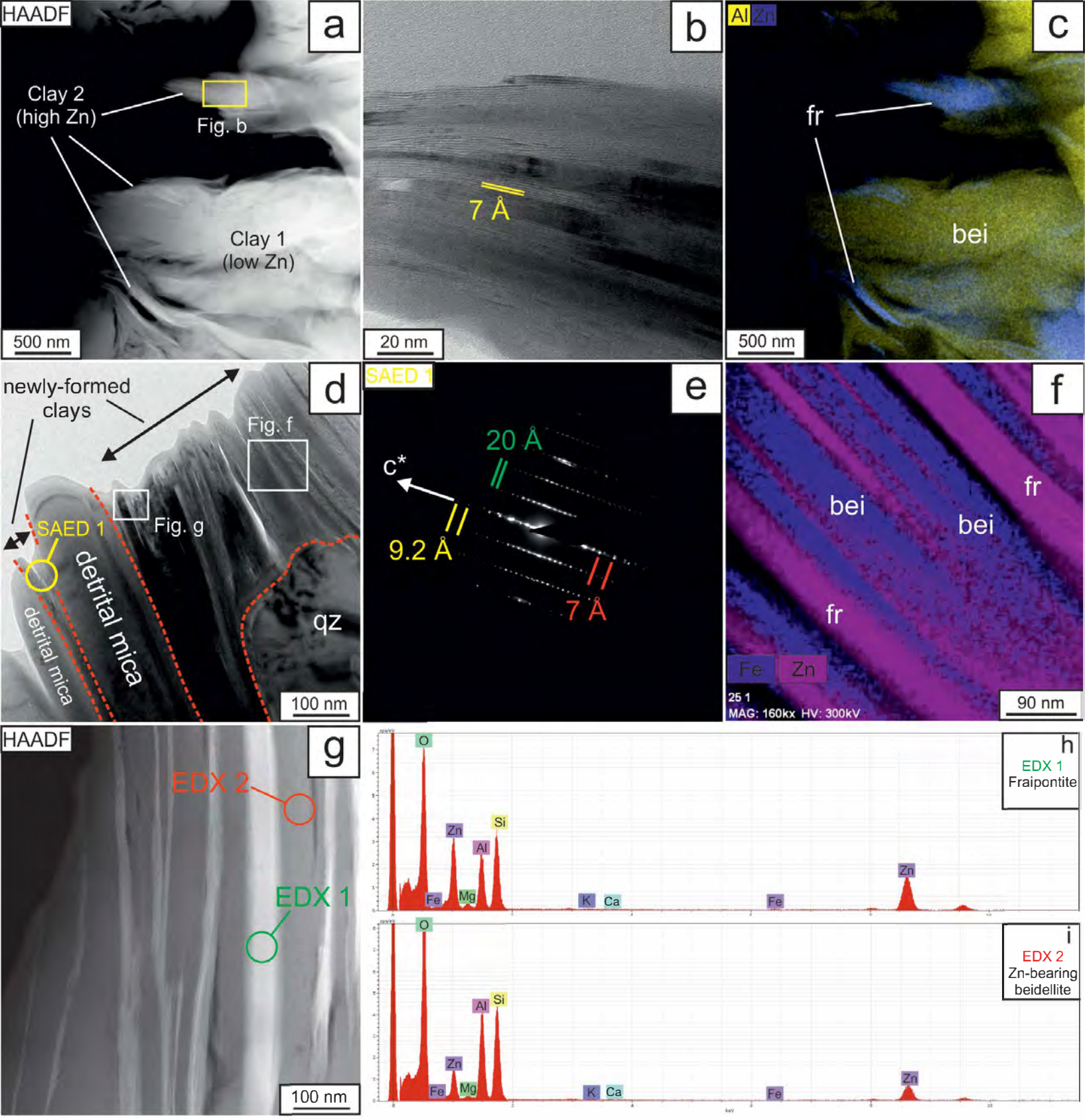
HAADF
a
Clay 2
(high Zn)
Fig. b
Clay 1
(low Zn)
500 nm
b
7 Å
20 nm
Al Zn
c
fr
bei
500 nm
newly-formed
clays
d
Fig. f
Fig. g
SAED 1
detrital mica
detrital mica
qz
100 nm
SAED 1
e
20 Å
c*
9.2 Å
7 Å
f
bei
fr
bei
fr
Fe
Zn
25 1
MAG: 160kx HV: 300kV
90 nm
HAADF
g
EDX 2
EDX 1
100 nm
O
Zn
Si
Al
Fe
Mg
K
Ca
Fe
Zn
h
EDX 1
Fraipontite
O
Al
Si
Zn
Fe
Mg
K
Ca
Fe
Zn
i
EDX 2
Zn-bearing
beidellite

Fig. 10

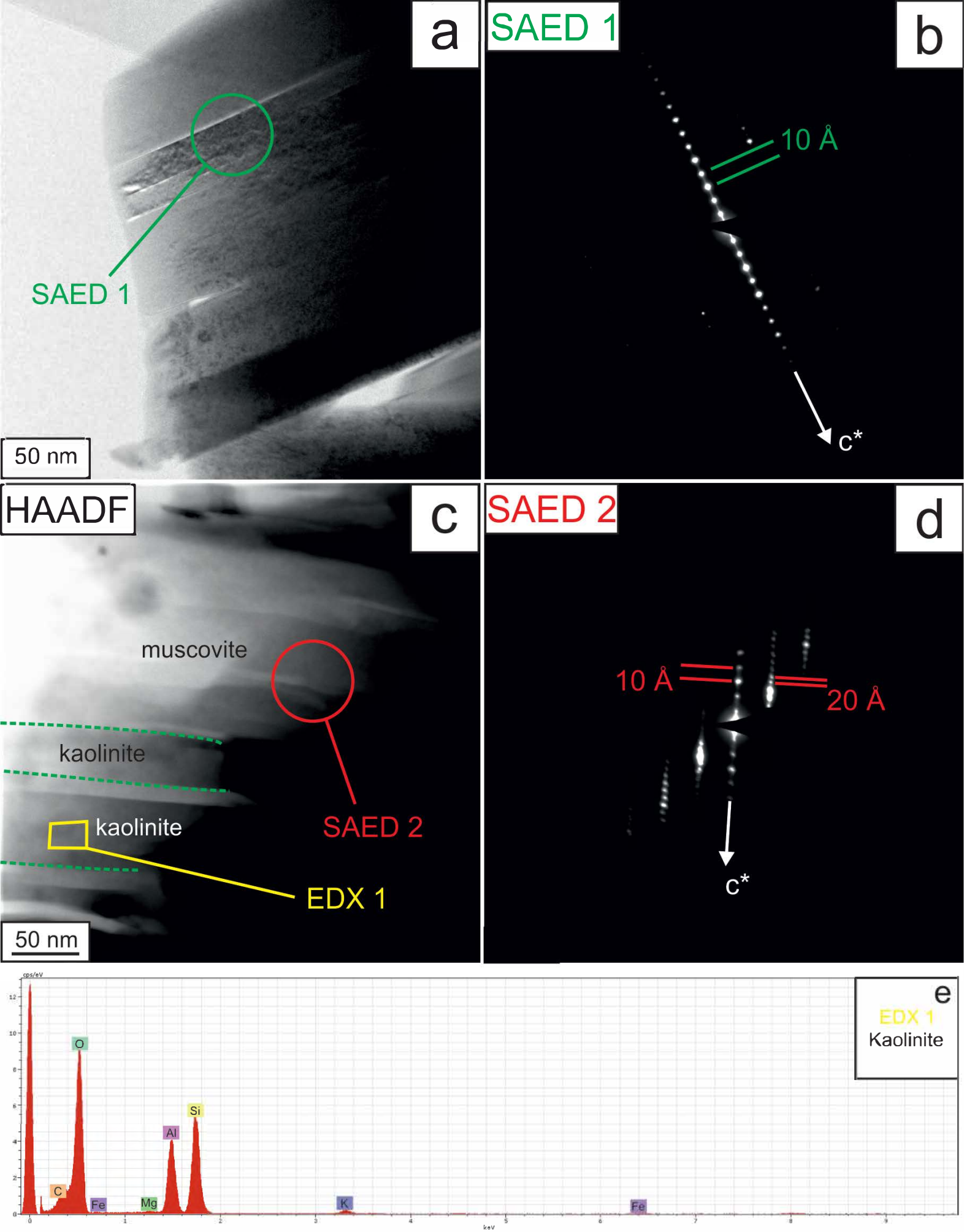
a
SAED 1
50 nm
SAED 1
b
10 Å
c*
HAADF
c
muscovite
kaolinite
kaolinite
SAED 2
EDX 1
50 nm
SAED 2
d
10 Å
20 Å
c*
e
EDX 1
Kaolinite
cps/eV
O
C
Fe
Mg
Al
Si
K
Fe
keV

Fig. 11

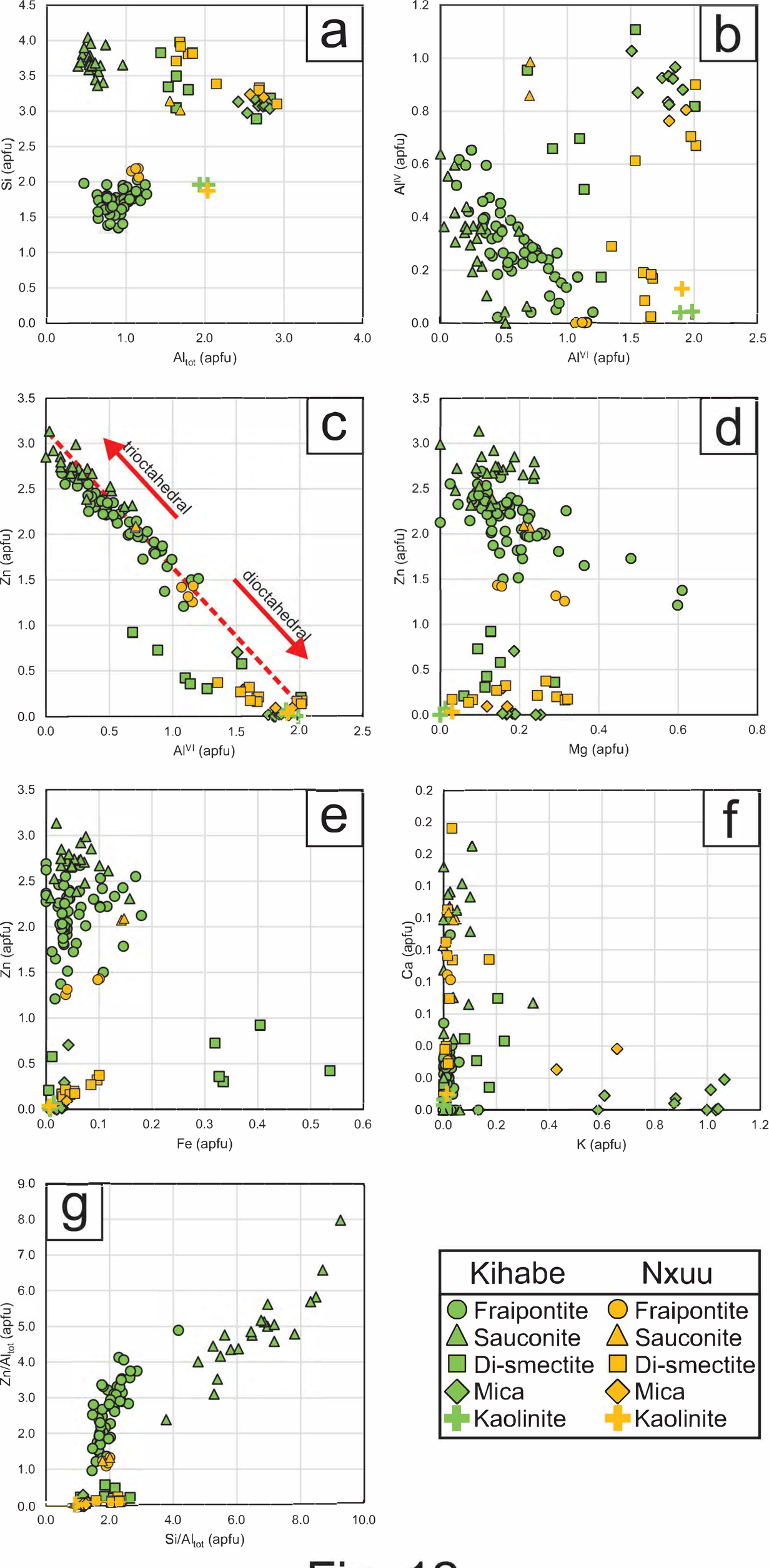
a
Si (apfu)
Al_{tot} (apfu)
b
Al^{IV} (apfu)
Al^{VI} (apfu)
c
trioctahedral
dioctahedral
Zn (apfu)
Al^{VI} (apfu)
d
Zn (apfu)
Mg (apfu)
e
Zn (apfu)
Fe (apfu)
f
Ca (apfu)
K (apfu)
g
Zn/Al_{tot} (apfu)
Si/Al_{tot} (apfu)
Kihabe
Nxuu
Fraipontite
Sauconite
Di-smectite
Mica
Kaolinite
Fraipontite
Sauconite
Di-smectite
Mica
Kaolinite

Fig. 12

Kihabe	Nxuu
Fraipontite	Fraipontite
Sauconite	Sauconite
Di-smectite	Di-smectite
Mica	Mica
Kaolinite	Kaolinite

M^+

$4Si = Si/4$

$M^+ = K+Na+2Ca$

$3R^{2+} = (Mg+Fe^{2+}+Zn)/3$

M

H

S

F

K

B

a

b

c

d

e

f

g

h

i

j

4Si

$3R^{2+}$

Fig. 13

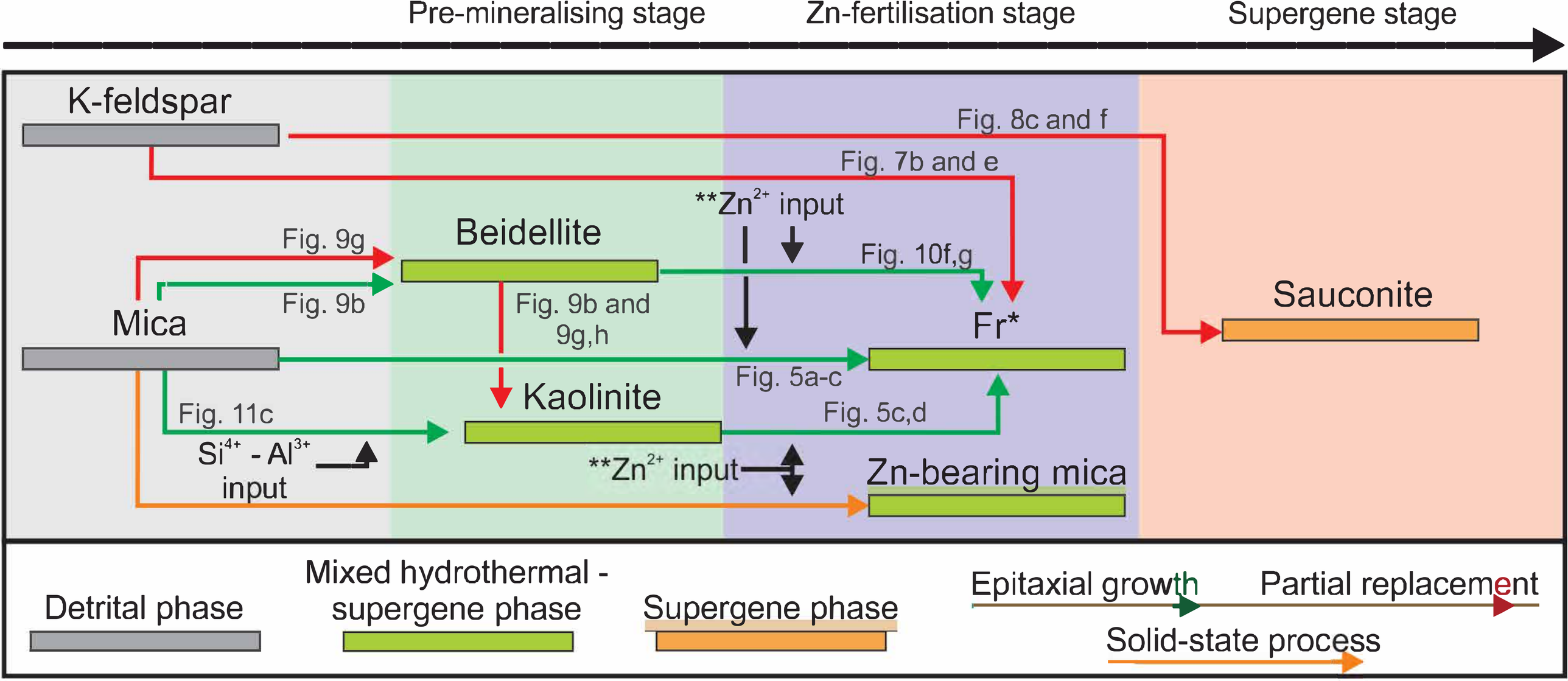
Pre-mineralising stage
Zn-fertilisation stage
Supergene stage
K-feldspar
Fig. 8c and f
Fig. 7b and e
**Zn2+ input
Fig. 9g
Beidellite
Fig. 10f,g
Fig. 9b
Fig. 9b and 9g,h
Mica
Fr*
Sauconite
Fig. 5a-c
Kaolinite
Fig. 11c
Fig. 5c,d
Si4+ - Al3+ input
**Zn2+ input
Zn-bearing mica
Detrital phase
Mixed hydrothermal - supergene phase
Supergene phase
Epitaxial growth
Partial replacement
Solid-state process

Fig. 14